Assessing General Circulation Model Simulations of Atmospheric Teleconnection Patterns

ANNE MARIE K. STONER

Department of Atmospheric Sciences, University of Illinois at Urbana–Champaign, Urbana, Illinois

KATHARINE HAYHOE

Department of Geosciences, Texas Tech University, Lubbock, Texas

DONALD J. WUEBBLES

Department of Atmospheric Sciences, University of Illinois at Urbana–Champaign, Urbana, Illinois

(Manuscript received 11 April 2008, in final form 12 March 2009)

ABSTRACT

The ability of coupled atmosphere–ocean general circulation models (AOGCMs) to simulate variability in regional and global atmospheric dynamics is an important aspect of model evaluation. This is particularly true for recurring large-scale patterns known to be correlated with surface climate anomalies. Here, the authors evaluate the ability of all Intergovernmental Panel on Climate Change (IPCC) Fourth Assessment Report (AR4) historical Twentieth-Century Climate in Coupled Models (20C3M) AOGCM simulations for which the required output fields are available to simulate three patterns of large-scale atmospheric internal variability in the North Atlantic region: the Arctic Oscillation (AO), the North Atlantic Oscillation (NAO), and the Atlantic multidecadal oscillation (AMO); and three in the North Pacific region: the El Niño–Southern Oscillation (ENSO), the Pacific decadal oscillation (PDO), and the Pacific–North American Oscillation (PNA). These patterns are evaluated in two ways: first, in terms of their characteristic temporal variability and second, in terms of their magnitude and spatial locations.

It is found that historical total-forcing simulations from many of the AOGCMs produce seasonal spatial patterns that clearly resemble the teleconnection patterns resulting from identical calculation methods applied to reanalysis and/or observed fields such as the 40-yr ECMWF Re-Analysis, NCEP–NCAR, or Kaplan sea surface temperatures (SSTs), with the exception of the lowest-frequency pattern, AMO, which is only reproduced by a few models. AOGCM simulations also show some significant biases in both spatial and temporal characteristics of the six patterns. Many models tend to either under- or overestimate the strength of the spatial patterns and exhibit rotation about the polar region or east–west displacement. Based on spectral analysis of the time series of each index, models also appear to vary in their ability to simulate the temporal variability of the teleconnection patterns, with some models producing oscillations that are too fast and others that are too slow relative to those observed. A few models produce a signal that is too periodic, most likely because of a failure to adequately simulate the natural chaotic behavior of the atmosphere. These results have implications for the selection and use of specific AOGCMs to simulate climate over the Northern Hemisphere, with some models being clearly more successful at (i.e., displaying less bias in) simulating large-scale, low-frequency patterns of temporal and spatial variability over the North Atlantic and Pacific regions relative to others.

1. Introduction

Atmospheric dynamics have long been characterized in terms of repeating patterns or cycles, identified through observations of surface pressure, geopotential height fields, sea surface temperatures, etc. Although the exact timing and magnitude of long-term oscillations in teleconnection patterns is chaotic, driven by internal variability of the climate system or oceans, pattern statistics do exhibit regular features (including both temporal characteristics such as frequency and amplitude and spatial characteristics such as distribution and intensity).

Corresponding author address: Anne Marie K. Stoner, Dept. of Atmospheric Sciences, 105 S. Gregory St., Urbana, IL 61801.
E-mail: ahertel@atmos.uiuc.edu

DOI: 10.1175/2009JCLI2577.1

© 2009 American Meteorological Society

These patterns have implications for future change, as long-term shifts in the frequency and/or intensity of natural cycles could alter the range of surface climate conditions experienced in many locations around the world. For that reason, it is important to evaluate the ability of atmosphere–ocean general circulation models (AOGCMs) to reproduce these patterns, as a reasonable first assumption might be that the models best able to reproduce historical observed characteristics of teleconnection patterns might also be best able to simulate future changes. Here, we examine six of those patterns: the Arctic Oscillation (AO), the North Atlantic Oscillation (NAO), the Atlantic multidecadal oscillation (AMO), the El Niño–Southern Oscillation (ENSO), the Pacific decadal oscillation (PDO), and the Pacific–North American Oscillation (PNA).

a. Atlantic teleconnection patterns

The AO[1] is characterized by a seesaw of pressure anomalies between the Arctic Basin and the surrounding zonal ring at midlatitudes, with an average period of 6–12 months (e.g., Lorenz 1950; Kutzbach 1970; Wallace and Gutzler 1981; Trenberth and Paolino 1981; Thompson and Wallace 1998). The AO is currently defined as the leading empirical orthogonal function (EOF) of the monthly mean sea level pressure (SLP) in the Northern Hemisphere. Thompson and Wallace (1998) found the leading mode of variability in the sea level pressure to be highly correlated to geopotential height variations of the wintertime polar vortex at 50 hPa and thus to be a surface signature of upper-air circulation patterns. The positive phase of the AO is defined by anomalously high pressure at the midlatitudes and lower-than-normal pressure in polar regions, producing a strong polar vortex (Fig. 1a). The negative phase is characterized by the opposite pattern.

The NAO is currently defined as an oscillation in the geopotential height field between the polar regions of the North Atlantic Ocean and a zonal region between 35° and 40°N in the Atlantic, with an average period of 6–12 months (Walker and Bliss 1932; van Loon and Rogers 1978; Wallace and Gutzler 1981; Barnston and Livezey 1987; Hurrell 1996), and is a result of a net displacement of air between the Arctic and the midlatitude Atlantic. As illustrated in Fig. 1b, the NAO has one center of its pressure dipole located over Greenland and the other located in the central North Atlantic 35°–40°N zonal band. The positive phase of the NAO tends to drive storm systems across the Atlantic Ocean toward northern Europe, whereas the negative phase of the NAO tends to drive storm systems farther south toward southern Europe. With a correlation of 0.65 between annual AO and NAO time series, it has been proposed that the NAO is actually a manifestation of the AO (Cohen et al. 2005; Stephenson et al. 2006). However, several other studies (Ambaum et al. 2001; Rogers and McHugh 2002; Kodera and Kuroda 2004) find significant differences between the two patterns. Ambaum et al. (2001) found that the NAO reflects the correlations between the surface pressure variability at its centers of action, whereas that is not the case for AO. Rogers and McHugh (2002) found that rotated principle component analysis of the spring, summer, and fall SLP fields for 1946–98 revealed that NAO- and AO-like patterns occurred as separate regional patterns, forming the first and second principal components, respectively.

A slower and more subtle oscillation with a period of 65–70 yr and amplitude of several tenths of a degree, the AMO (Fig. 1c), has been identified in the North Atlantic Ocean sea surface temperatures (SSTs) (Bjerknes 1964; Schlesinger and Ramankutty 1994; Andronova and Schlesinger 2000; Kerr 2000; Delworth and Mann 2000; Enfield et al. 2001). Some speculate that this oscillation is a result of fluctuations of the intensity of the Atlantic thermohaline circulation and may even have influenced decadal temperature variations and the amplitude of El Niño–Southern Oscillation periods over the past century (Andronova and Schlesinger 2000; Delworth and Mann 2000; Mestas-Nuñez and Enfield 1999; Enfield et al. 2001). Hence, it is thought that the AMO might have a significant impact on global mean climate, although it has a lower frequency and is less obvious than other patterns.

b. Pacific teleconnection patterns

The El Niño–Southern Oscillation is a coupled atmospheric–oceanic oscillation in the tropical Pacific with an average period of 2–7 years, first described in 1923 by Sir Gilbert Walker (Walker 1923). During the positive El Niño phase, a tongue of anomalously warm surface water extends off the coast of Peru along the equator (Fig. 1d), driving changes in atmospheric circulation that strengthen the westerly jets north and south of the equator (see http://www.cpc.ncep.noaa.gov/products/analysis_monitoring/ensocycle/enso_circ.shtml). The opposite occurs under La Niña conditions. ENSO is one of the most important patterns of natural interannual variability in the climate system, influencing both average and extreme weather events (Timmermann et al. 1999; AchutaRao and Sperber 2002). Because of its frequent societal impacts, ENSO is arguably the most

[1] The AO is also known as the northern annular mode (NAM).

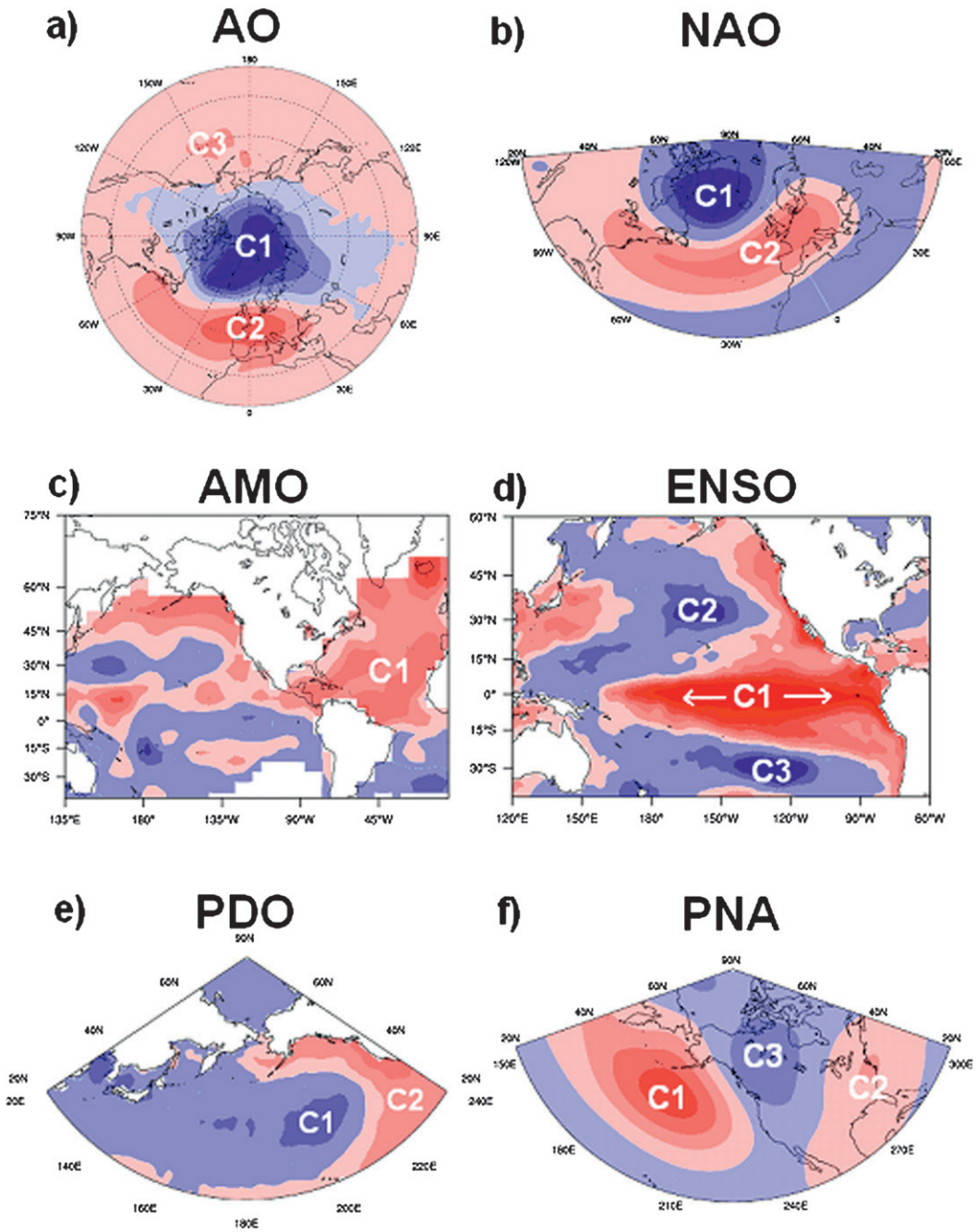

FIG. 1. Spatial patterns for (a) the AO (calculated from 950-hPa heights), (b) the NAO (calculated from 500-hPa heights), (c) the AMO (calculated from SST), (d) the ENSO (calculated from SST), (e) the PDO (calculated from SST), and (f) the PNA (calculated from 500-hPa heights) calculated from the ERA-40 (Kaplan for AMO) based time series, with terminology of regions analyzed. Values are slopes of the regression analyses.

studied mode of natural variability, to which the most attention has been paid regarding the ability of present-day AOGCMs to simulate it (AchutaRao and Sperber 2002, 2006; Cai et al. 2003; Davey et al. 2002; Latif et al. 2001; Li 1999; Min et al. 2005; van Oldenborgh et al. 2005; Straus and Shukla 2002).

Like ENSO, the PDO is dominated by oceanic temperature oscillations with a typical period of 20–30 years. Although PDO SST anomalies are smaller than ENSO anomalies, they occur over a much larger region—the PDO index is defined by Pacific SST anomalies poleward of 20°N (Mantua et al. 1997; Zhang et al. 1997; Nigam et al. 1999). Although the atmospheric and/or oceanic mechanisms driving the PDO are currently unknown, the typical PDO pattern is well defined. During the positive (negative) phase, waters in the east tropical Pacific and along the North American west coast are anomalously warm (cool) while waters in the northern, western, and southern Pacific are colder (warmer) than normal (Fig. 1e).

Finally, the PNA is driven by oscillations in geopotential height over the Pacific and across the North American continent (Wallace and Gutzler 1981). It is associated with fluctuations in the strength and location of the East Asian jet stream, and has a period of less than 1 year to about 4 years (see www.cpc.ncep.noaa.gov/data/teledoc/pna.shtml). The positive (negative) phase of the PNA is defined by above-average (below average) geopotential heights near Hawaii and in western Canada, and below-average (above average) heights south of the Aleutian Islands and in the southeastern United States (Fig. 1f). The positive phase is caused by an enhanced East Asian jet stream and an eastward shift of the exit region of the jet toward the western United States, while the negative phase is associated with a retraction of the jet toward East Asia (Wallace and Gutzler 1981).

c. *AOGCM simulation of teleconnection patterns*

Earlier studies have addressed the ability of AOGCMs to simulate specific teleconnection pattern events, with a particular focus on the ENSO phenomenon (AchutaRao and Sperber 2002, 2006; Cai et al. 2003; Davey et al. 2002; Latif et al. 2001; Li 1999; Min et al. 2005; van Oldenborgh et al. 2005; Straus and Shukla 2002), NAO (Bojariu and Gimeno 2003; Cohen et al. 2005; Corti et al. 1997; Graham et al. 2005; Hurrell et al. 2006; Huth 1997; McHugh and Rogers 2005; Min et al. 2005; Osborn et al. 1999; Schoof and Pryor 2006; Stephenson and Pavan 2003; Stephenson et al. 2006), and PNA (Corti et al. 1997; Derome et al. 2005; Schoof and Pryor 2006; Straus and Shukla 2002). Few studies have examined the AO (Hurrell et al. 2006; Miller et al. 2006), the AMO pattern (Andronova and Schlesinger 2000; Delworth and Mann 2000), and the PDO (Overland and Wang; Wang et al. 2009). Of these studies, most examine only the ability of one or two AOGCMs to simulate one or, at most, two patterns of variability.

In general, most studies find that both uncoupled and coupled AOGCMs capture the AO, NAO, ENSO, and PNA patterns well. Previous analyses have identified intermodel differences and systematic biases relative to observations, including an overestimation of the magnitude of the spatial pattern (Stephenson et al. 2006), displacement or rotation of the pattern (AchutaRao and Sperber 2006; Cai et al. 2003; Min et al. 2005; van Oldenborgh et al. 2005; Randall et al. 2007), and too frequent and regular temporal variability (Min et al. 2005; van Oldenborgh et al. 2005).

A number of more comprehensive analyses reveal further nuances. In the Atlantic, for example, Cohen et al. (2005) compared NAO simulations by models from the Atmospheric Model Intercomparison Project Phase 2 (AMIP-2) forced by observed SSTs. This work revealed that the influence of SSTs on the phase of the NAO at interannual time scales was trivial compared to the influence from stochastic variations. Simulations by 10 perturbed AOGCMs by McHugh and Rogers (2005) showed that models successfully reproduced the observed NAO SLP and temperature anomaly fields, but model control SLP anomaly fields more closely resembled AO than NAO because of expansion of the North Atlantic low pressure area. Miller et al. (2006) found that AOGCM-based AO spatial patterns for 14 models were strongly correlated with observed (near or above 85% in winter) but tended to overestimate the percentage of total temporal variability in Northern Hemisphere SLPs accounted for by the AO; similar results were found by Stephenson et al. (2006) using phase 2 of the Coupled Model Intercomparison Project (CMIP2) models. Finally, although simulations of the AMO are limited, the pattern has been identified in a 1400-yr control simulation from the third climate configuration of the Met Office Unified Model (UKMO HadCM3) (Knight et al. 2006), although with a smaller variability than observed.

In the Pacific, AchutaRao and Sperber (2006), Cai et al. (2003), Min et al. (2005), and van Oldenborgh et al. (2005) all found that models tend to simulate an ENSO pattern extending too far west across the tropical Pacific, perhaps because many of the AOGCMs have a tendency to produce a split ITCZ over the west Pacific (AchutaRao and Sperber 2006). In terms of the implications of this shortcoming, Cai et al. (2003) found that, for the Commonwealth Scientific and Industrial Research Organisation Mark version 3.0 (CSIRO

Mk3.0) model, rainfall climatology over the tropical ocean is affected by the westward shift of the pattern, especially in Indonesia and northeast Australia, but not teleconnections to ENSO elsewhere. Min et al. (2005) and van Oldenborgh et al. (2005) found that some models [ECHAM and the global Hamburg Ocean Primitive Equation (ECHO-G); Centre National de Recherches Météorologiques Coupled Global Climate Model, version 3 (CNRM-CM3); Flexible Global Ocean–Atmosphere–Land System Model gridpoint version 1.0 (FGOALS-g1.0); and L'Institut Pierre-Simon Laplace Coupled Model, version 4 (IPSL CM4)] simulate ENSO temporal variability that is too frequent and too regular, as opposed to the more irregular observed ENSO variability, whereas the ECHAM/Max Planck Institute Ocean Model (MPI-OM), Geophysical Fluid Dynamics Laboratory Climate Model version 2.1 (GFDL CM2.1), Model for Interdisciplinary Research on Climate 3.2 (MIROC3.2), and UKMO HadCM3 display more realistic temporal properties (van Oldenborgh et al. 2005). Overland and Wang (2007) and Wang et al. (2009) studied the ability of the Intergovernmental Panel on Climate Change (IPCC) Fourth Assessment Report (AR4) models to reproduce the twentieth century temporal and spatial variability of the PDO pattern. They found that 12 of the 23 models were able to simulate a recognizable pattern both temporally and spatially.

The PNA was studied by Corti et al. (1997) and Derome et al. (2005) using more primitive models; however, both found these to be surprisingly accurate, although the PNA occupies a slightly wider region than observed. Comparing coupled AOGCM simulations, Schoof and Pryor (2006) found that UKMO HadCM3 and Canadian Centre for Climate Modelling and Analysis (CCCma) Coupled General Circulation Model version 2 (CGCM2) were both relatively successful at simulating the PNA.

Although AOGCM ability to simulate individual teleconnection patterns has been evaluated previously (and in great detail, in the case of ENSO), our study is unique in that we examine 22 of the AOGCMs that submitted simulations to the IPCC AR4 and focus simultaneously on three patterns of variability in the North Atlantic and three in the Pacific. We believe that it is an important step in the evaluation of AOGCMs to obtain a broad overview of the capabilities and weaknesses of each model as well as the entire suite of AR4 models. To that end, section 2 of this paper describes the model simulations and calculation methods used. Sections 3 and 4 compare temporal and spatial characteristics of AOGCM-based simulations of each pattern with reanalysis-based patterns. In section 5 we draw some general conclusions regarding AOGCM ability to simulate these important atmospheric circulation features and explore the implications of their abilities (or lack thereof) to reproduce key features of the climate system.

2. Model simulations and calculation methods

a. Reanalysis

We compare historical AOGCM simulations to two-sets of quasi-observational upper-air and sea surface temperature variables obtained from the 40-yr European Centre for Medium-Range Weather Forecasts (ECMWF) Re-Analysis (ERA-40) output fields generated by the ECMWF Integrated Forecast System (IFS) C423r4 model (at a resolution of 1.125° × 1.125° and 60 levels in the vertical; Kållberg et al. 2004), and from the National Centers for Environmental Prediction–National Center for Atmospheric Research (NCEP–NCAR) reanalysis project (with a T62 resolution, which implies a horizontal grid scaling of about 210 km or about 2.5° × 2.5° grid spacing). Analyses were produced daily at 0000, 0600, 1200, and 1800 UTC beginning in September 1957 and ending in August 2002 for ERA-40 and from 1948 until the present for NCEP; however, for short-period indices we use only the period from January 1960 to December 1999 to maintain a consistent 40-yr period. ERA-40 geopotential fields were further interpolated to geopotential height to match NCEP–NCAR and AOGCM output fields.

Long-term sea surface temperatures were not available from NCEP–NCAR; hence, when sea surface temperatures were required, we used the Kaplan extended SST V2 data provided by the National Oceanic and Atmospheric Administration/Office of Oceanic and Atmospheric Research/Earth System Research Laboratory (NOAA/OAR/ESRL) Physical Sciences Division (PSD) (see http://www.cdc.noaa.gov), which extends back to 1856 (Kaplan et al. 1998). The dataset provides global mean monthly SST anomaly values at 5° × 5° grid, with anomalies based on 1951–80. This dataset is based on the Met Office Historical Sea Surface Temperature Anomalies (MOHSST5) version of the Global Ocean Surface Temperature Atlas (GOSTA) dataset.

A slight warm bias has been noted in the ERA-40 dataset, mainly in springtime (see http://www.ecmwf.int/research/era/Data_Services/section3.html), and a slight cold bias has been noted in summertime, associated with too much evaporation (see http://knik.iarc.uaf.edu/atmgroup/workshop_announcement/nwp_polar_2003_pedro.ppt). Studies (Trigo 2006; Sterl 2004) have also shown discrepancies between the ERA-40 and NCEP reanalysis datasets, with ERA-40 being overall slightly better than NCEP in reproducing observations. This is thought to

be mainly due to the difference in resolution (Trigo 2006). Discrepancies have also been found between all three reanalysis datasets and station observations, especially in the earlier part of the period because of input from fewer stations than in the latter part of the period (Sterl 2004). Nevertheless, owing to their high resolution and frequent forcing by observed data, reanalysis output fields provide the closest approximation to observed large-scale atmospheric circulation fields available for that time period. It must be noted, however, that some part of the differences between AOGCMs and reanalysis fields may be due to the inability of reanalysis fields to accurately capture reality, not only the failure of the AOGCMs to simulate it.

b. *Atmosphere–ocean general circulation models*

To assess the ability of the latest AOGCMs to simulate the six teleconnection patterns examined here, we rely on historical simulations from the IPCC AR4 database (http://www.earthsystemgrid.org) for the 22 models for which monthly SSTs and 500- and 925-hPa geopotential height fields are available. Model provenance, resolution, and key references are provided in Table 1.

Historical simulations correspond to the CMIP Twentieth-Century Climate in Coupled Models (20C3M) scenarios (Covey et al. 2003). These represent each modeling group's best efforts to simulate observed climate over the past century. Although the 20C3M simulations are all intended to represent the same historical total-forcing scenarios (including both natural variability as well as the effect of human emissions on climate), simulations by individual modeling groups do not necessarily have identical boundary conditions. Therefore, some differences between model simulations themselves as well as between simulations and observations identified here may also be a result of differing input conditions. Some modeling centers provide multiple members of the twentieth-century runs, when this was the case "run 1" was used in the analysis.

c. *Teleconnection index calculation methods*

To evaluate the ability of the AOGCMs to simulate the six Northern Hemisphere teleconnection patterns, we characterize each oscillation in two ways. The first is temporal, calculating the monthly time series for each teleconnection pattern from ERA-40 and NCEP or Kaplan reanalysis fields and AOGCM output fields. The second is spatial, deriving the seasonal spatial patterns corresponding to each teleconnection pattern by regressing the time series on the original fields used to generate the index.

To calculate the AO index time series, we rely on the Climate Prediction Center (CPC) procedure that defines the AO as the leading eigenvector of monthly mean 1000-hPa geopotential height anomalies poleward of 20°N. To reduce the number of missing values due to model topography, 925-hPa geopotential heights were substituted for 1000 hPa, except for in the HadCM3 model, where 950 hPa was used instead. As for the remainder of the indices as well, seasonality was removed based on the climatology for the time period 1960–99. Gridded data was area weighted and the resulting eigenvector standardized by the 10-yr running standard deviation, to allow for changes in standard deviation, and any linear and quadratic trends were removed.

Several calculation methods are commonly used for the NAO index time series. For example, Barnston and Livezey (1987) developed a method that performs a rotated principal component analysis (RPCA) on 700-hPa geopotential heights. This method is applied to 500-hPa fields by the CPC. Hurrell (1995) defined the NAO as the difference in sea level pressure between Lisbon, Portugal and Stykkisholmur/Reykjavik, Iceland. Others (Cohen et al. 2005; Stephenson and Pavan 2003) have used a principal component analysis (PCA) approach applied to North Atlantic SLP or SST, while Corti et al. (1997) applied PCA to North Atlantic 500-hPa geopotential heights.

To determine which of these methods would be most effective in identifying NAO patterns in AOGCM output fields, we computed NAO index time series in four different ways from the ERA-40 reanalysis fields (using closed grid cells for station-based method) and correlated these with the CPC NAO index. As we found the Corti et al. (1997) version to be correlated most closely with the CPC time series ($r = 0.82$), it was used to calculate both reanalysis and AOGCM-based NAO time series and patterns used in this study based on 500-hPa output fields. Using a higher level of data (500 hPa versus SLP) likely reduced the noise in the data, as SLP fields tend to be more strongly affected by local features than midtropospheric geopotential height fields.

The AMO index time series is simply the weighted monthly mean of the SSTs in the North Atlantic Ocean between 0°–70°N (Enfield et al. 2001). Some models did not provide SST fields to the IPCC AR4 database [Beijing Climate Center Climate model version 1 (BCC-CM1), ECHAM5/MPI-OM, and CNRM-CM3]; hence it was not possible to do an AMO analysis for these.

A range of oceanic regions and metrics are used to calculate the ENSO index (Smith and Sardeshmukh 2000; Trenberth and Hoar 1996; Trenberth 1997). Here, reanalysis- and AOGCM-based time series of the ENSO index are derived by calculating the monthly area-weighted mean of SST anomalies in the Niño-3.4 region (5°N–5°S, 170°–120°W) as defined in Trenberth (1997),

TABLE 1. Summary of key characteristics of AOGCMs used, including acronyms, host institution, atmospheric and oceanic resolution, and the primary reference for each.

Model acronym	Host institution	Resolution		Start year (SST)	Reference
		Atmospheric	Oceanic		
BCC-CM1	Beijing Climate Center (China)	1.9° × 1.9°	1.9° × 1.9°	N/A	(CSMD 2005)
BCCR-BCM2.0	Bjerknes Centre for Climate Research (Norway)	1.9° × 1.9°	0.5°–1.5° × 1.5°	1850	(Furevik et al. 2003)
CCSM3	National Center for Atmospheric Research (United States)	1.4° × 1.4°	0.3°–1.0° × 1.0°	1870	(Collins et al. 2006)
CGCM3.1 (T47)	Canadian Centre for Climate Modeling and Analysis (Canada)	2.8° × 2.8°	1.9° × 1.9°	1850	(Flato 2005)
CGCM3.1 (T63)	Canadian Centre for Climate Modeling and Analysis (Canada)	1.9° × 1.9°	0.9° × 1.4°	1850	(Flato 2005)
CNRM-CM3	Météo-France/Centre National de Recherches Météorologiques (France)	1.9° × 1.9°	0.5°–2.0° × 2.0°	N/A	(Salas-Mélia et al. 2005)
CSIRO Mk3.0	Commonwealth Scientific and Industrial Research Organization (CSIRO) Atmospheric Research (Australia)	1.9° × 1.9°	0.8° × 1.9°	1871	(Gordon et al. 2002)
ECHAM5/MPI-OM*	Max Planck Institute for Meteorology (Germany)	1.9° × 1.9°	1.5° × 1.5°	N/A	(Roeckner et al. 2003)
FGOALS-g1.0	National Key Laboratory of Numerical Modeling for Atmospheric Sciences and Geophysical Fluid Dynamics (LASG)/Institute of Atmospheric Physics (China)	2.8° × 2.8°	1.0° × 1.0°	1850	(Yu et al. 2002 2004)
GFDL CM2.0	U.S. Department of Commerce/NOAA/GFDL (United States)	2.0° × 2.5°	0.3°–1.0° × 1.0°	1861	(Delworth et al. 2006)
GFDL CM2.1	NOAA/GFDL (United States)	2.0° × 2.5°	0.3°–1.0° × 1.0°	1861	(Delworth et al. 2006)
GISS-AOM	National Aeronautics and Space Administration (NASA)GISS (United States)	3° × 4°	3° × 4°	1850	(Russell et al. 1995; Russell 2005)
GISS-EH	NASAGISS (United States)	4° × 5°	2° × 2°	1880	(Schmidt et al. 2006)
GISS-ER	NASAGISS (United States)	4° × 5°	4° × 5°	1880	(Schmidt et al. 2006)
INM-CM3.0	Institute for Numerical Mathematics (Russia)	4° × 5°	2° × 2.5°	1871	(Diansky and Volodin 2002; Diansky et al. 2002)
IPSL CM4	L'Institut Pierre-Simon Laplace (France)	2.5° × 3.75°	2° × 2°	1860	(Hourdin et al. 2006)
MIROC3.2(hires)	Center for Climate System Research (University of Tokyo), National Institute for Environmental Studies, and Frontier Research Center for Global Change [Japan Agency for Marine-Earth Science and Technology (JAMSTEC)] (Japan)	1.1° × 1.1°	0.2° × 0.3°	1900	(Hasumi and Emori 2004)
MIROC3.2(medres)	Center for Climate System Research (University of Tokyo), National Institute for Environmental Studies, and Frontier Research Center for Global Change (JAMSTEC) (Japan)	2.8° × 2.8°	0.5°–1.4° × 1.4°	1850	(Hasumi and Emori 2004)
MRI CGCM2.3.2	Meteorological Research Institute (Japan)	2.8° × 2.8°	0.5°–2.0° × 2.5°	1901	(Yukimoto et al. 2001; Yukimoto and Noda 2003)
PCM	NCAR (United States)	2.81° × 2.81°	0.5°–0.7° × 1.1°	1890	(Washington et al. 2000)
UKMO HadCM3	Hadley Centre for Climate Prediction and Research/Met Office (United Kingdom)	2.5° × 3.75°	1.25° × 1.25°	1860	(Gordon et al. 2000; Pope et al. 2000)
UKMO HadGEM1	Hadley Centre for Climate Prediction and Research/Met Office (United Kingdom)	1.3° × 1.9°	0.3°–1.0° × 1.0°	1860	(Johns et al. 2006; Martin et al. 2006)

* This model incorporates flux adjustment, an artificial component added to the model to improve simulation of sea–air energy fluxes.

as this region has proven to have a stronger signal and higher correlation with the Southern Oscillation index.

The PDO is defined as the leading eigenvector of monthly North Pacific SSTs (Mantua et al. 1997), where the North Pacific area is defined as being the area contained within the latitudes 20°–90°N and longitudes 110°–110°W. Eigen analysis was performed on the SST covariance matrix to find the leading eigenvector, which was again standardized and any linear and quadratic trends removed.

Similarly to the NAO, there are several ways of defining the PNA. It was first defined by Wallace and Gutzler (1981), based on a linear combination of the normalized geopotential height anomalies at four centers of action at 500 hPa. However, Barnston and Livezey (1987) developed a RPCA method to calculate the PNA index, applied to SLP and 500-hPa geopotential heights, which is the preferred method by the CPC.

Given the different calculation methods for PNA, we again compared four different methods applied to ERA-40 reanalysis fields against the CPC PNA time series (again using closed grid cells for station-based methods). We found the PCA-based method using 500-hPa geopotential heights to show the highest correlation with the CPC time series ($r = 0.73$). The PCA-based method using 500-hPa geopotential heights was therefore chosen to calculate the PNA index time series from ERA-40 and AOGCM output fields.

Given the time series for each of the six patterns, we then derive a distinctive spatial pattern, comparable to EOFs, for each of the teleconnection indices as simulated by the reanalyses and AOGCMs through projecting the time series back onto the original fields used to generate the time series of the index [Northern Hemisphere 925-hPa geopotential height (ZG925) or ZG950 for AO, North Atlantic ZG500 for NAO, and SSTs for AMO, Pacific SSTs for ENSO, North Pacific SSTs for PDO, and ZG500 for PNA] using regression techniques for AO, NAO, ENSO, PDO, and PNA and correlation analysis for AMO. In generating the patterns, seasonality was removed from both the time series and the geopotential height/SST fields as described previously, and the data (both gridded data and the time series) were divided into four seasons [December–February (DJF), March–May (MAM), June–August (JJA), and September–November (SON)] to analyze seasonal variability in the patterns. Since the AMO is a multidecadal oscillation, only the annual patterns were derived for this analysis. Each grid cell, consisting of a time series of seasonal-averaged values, was then regressed on the index time series to obtain the slope of the regression. This reveals both the sign of the correlation as well as the magnitude of any anomalies, and is an estimate of how the time series of values for each grid cell change as a linear function of the index time series. When regression slopes are plotted, the resulting map reveals the teleconnection pattern for each index.

3. Comparison of temporal variability

We first quantitatively compare the temporal variability of reanalysis- and AOGCM-based time series by calculating the power spectrum for each time series. Figures 2a–f show the power spectra for each model for the six teleconnection patterns. (Time series and individually color coded power spectra for all six patterns and 22 AOGCMs can be found at http://temagami.tosm.ttu.edu/~ahertel/teleconnection/. Here individual models are not distinguishable from one another.)

a. Temporal variability of AOGCM-simulated Atlantic indices

For the AO, spectral analysis (Fig. 2a) of both ERA-40 and NCEP reanalysis-based time series indicate the annular and semiannular behavior of this pattern. Most AOGCM-based time series capture the semiannular, but not the annular, behavior; however, there is a tendency for the models to also exhibit a peak near 24 months. Furthermore, most models show signs of seasonality with small peaks near 3 and 9 months as well as a lower-frequency variability ranging from 18 to about 30 months, not seen in the observed time series. Specifically, the Community Climate System Model, version 3 (CCSM3); FGOALS-g1.0; Goddard Institute for Space Studies Model E-H (GISS-EH); IPSL CM4; UKMO HadCM3; and Hadley Centre Global Environmental Model version 1 (UKMO HadGEM1) are the only models that have a periodic component near 12 months, as seen in the observations. These six models also display the observed peak at about 6 months.

Given the connection of the AO to the strength and position of the polar vortex, the fact that many models simulate the AO with a higher or lower variability than observed suggests their simulation of the variability of the polar vortex may be affected as well. The length of positive and negative phases of the AO affects the period of time that storm tracks persist over either the northern North Atlantic/Pacific (positive phase) or the southern North Atlantic/Pacific (negative phase). Thus, models with higher rates of internal variability might be expected to have shorter-lived weather patterns associated with positive and negative phases of the AO; similarly, models with longer-lasting positive and negative phases might be expected to simulate more persistent weather patterns than observed.

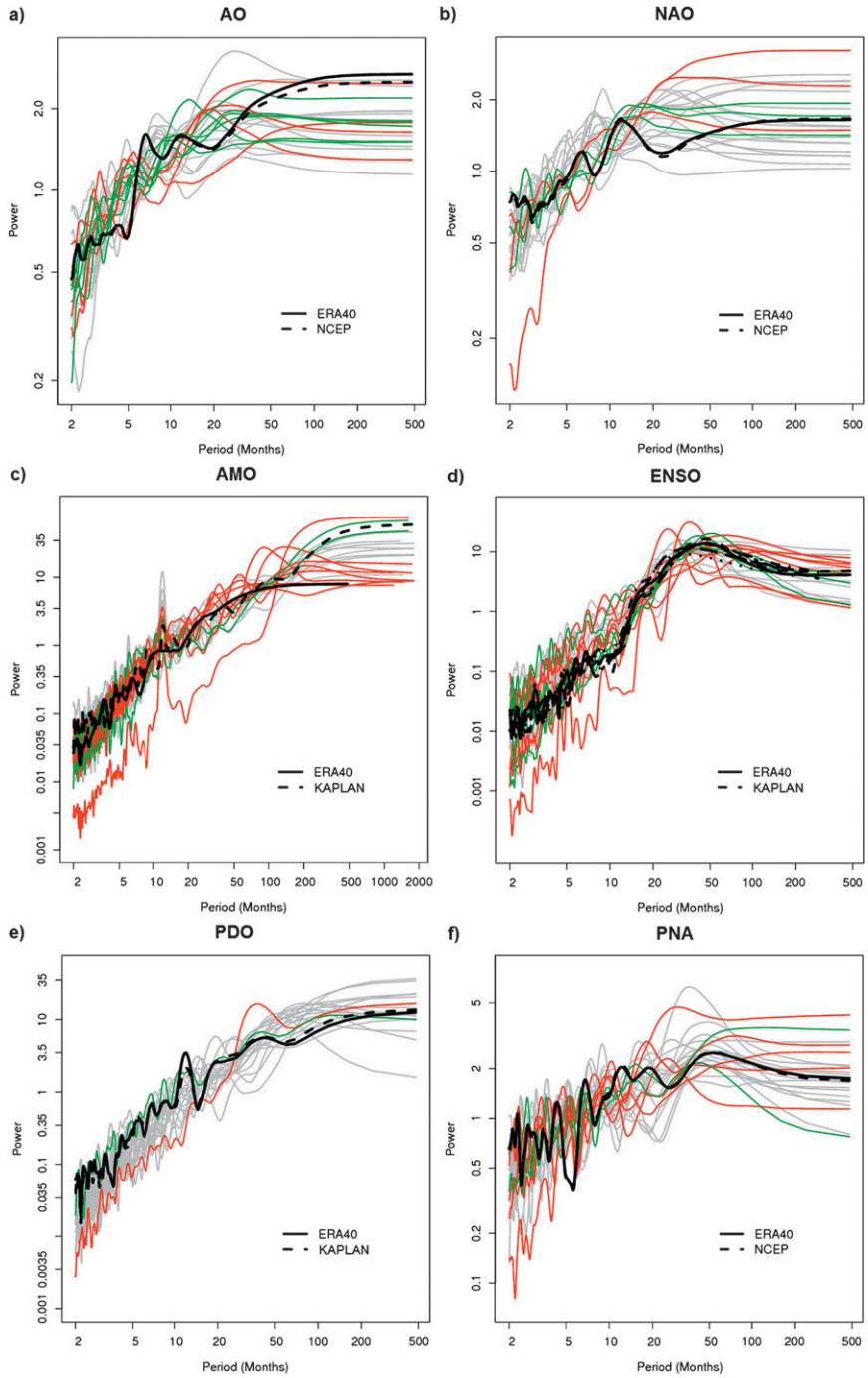

FIG. 2. Smoothed power spectrum for the unsmoothed 1960–99 time series of (a) AO, (b) NAO, (c) AMO, (d) ENSO, (e) PDO, and (f) PNA. ERA-40 and NCEP/Kaplan reanalysis are in black (solid and dashed curves, respectively), and AOGCM simulations are in gray or color depending on their performance in simulating the temporal variability. Green: the model is capable of reproducing a temporal variability that closely resembles the observations. Gray: the model is able to produce a recognizable temporal variability, albeit one with significant differences relative to the observations. Red: the model is not able to produce a recognizable temporal variability.

The NAO power spectra for both reanalysis data and model simulations are shown in Fig. 2b. Both reanalysis datasets show semiannular and annular behavior, while, similar to AO, AOGCM simulations exhibit peaks of both shorter (3–4 month) and longer (24 months) frequency than reanalysis. Only CCSM3, UKMO HadCM3, and UKMO HadGEM1 have two peaks near 6 and 12 months, as observed. These three models also compared well with observations for the temporal variability of the AO. Half of the models also exhibit a peak near 9 months, which cannot be found in the reanalysis data.

As with the model simulations of the AO time series, the fact that most of the models poorly simulate the NAO temporal variability suggests that these models may have difficulties simulating the temporal variability of the dynamical features causing the NAO as well as the atmospheric dynamics that the NAO affects. Some of the most important features affected by the NAO include the position of the North Atlantic jet stream and thus the tracks of midlatitude cyclones over the North Atlantic Ocean. These primarily affect winter weather in Europe and Scandinavia, suggesting a poorer predictability of European winter weather by models that poorly simulate the NAO.

Since the AMO teleconnection pattern has such a long periodicity, we compared AOGCM SST time series calculated from the beginning of each model's SST record for the 20C3M simulation, which ranges from 1850 to 1901, to observed AMO time series derived from the Kaplan SST dataset. Few models appear able to reproduce the approximately 70-yr periodicity of the AMO pattern (only slightly evident in the Kaplan dataset) over this time scale (Fig. 2c); however, two of the AOGCMs do display similar peaks [CCSM3 and Institute of Numerical Mathematics Coupled Model, version 3.0 (INM-CM3.0)]. The majority of the models, however, produce an AMO-like oscillation on a much shorter time scale than the generally observed 70-yr oscillation (Enfield et al. 2001). Furthermore, many models display a strong peak near 12 months (the Kaplan dataset also shows a small peak at this time). This is most likely an artifact driven by either the AO or NAO oscillation. The remaining AOGCMs range from having a slight resemblance to observations to performing relatively poorly (see Fig. 9).

The fact that so few of the models can reproduce the temporal variability of the AMO pattern is most likely due to the subtlety of the oscillation as well as the short length of the datasets relative to the oscillation period. The AMO is thought to be driven by heat-carrying currents in the oceans; hence, failing to reproduce an AMO-like oscillation, models are most likely reflecting their limitations in reproducing these currents. This bias could have implications for predicting precipitation over the landmasses bordering the Atlantic Ocean, as well as oceanic heat transport, which is key to resolving the impact of climate change on the thermohaline circulation in the Atlantic.

b. Temporal variability of AOGCM-simulated Pacific indices

Spectral analysis of the ERA-40 and Kaplan-based ENSO time series (Fig. 2d) show a peak between approximately 2 and 7 yr, corresponding to the range of observed oscillation period of this pattern. When the observed time series are divided into pre- and post-1976 (Fig. 2d), the 1976 tropical Pacific regime shift documented in earlier studies is evident (not shown here, but available at http://temagami.tosm.ttu.edu/~ahertel/teleconnection/), with longer periods pre-1976 and shorter thereafter (Quinn and Neal 1984, 1985; Nitta and Yamada 1989; Trenberth and Hoar 1996; Wang and Wang 1996; Zhang et al. 1997; Guilderson and Schrag 1998; Kestin et al. 1998; Karspeck and Cane 2002). Only four of the 19 AOGCM-based ENSO time series (three AOGCMs did not provide SSTs) reproduce a spectral peak between 2 to 7 yr. Eight models display peaks earlier than observed, with the largest peak near 2 yr, indicating a time series that is oscillating more rapidly than even the post-1976 observed periodicity. In particular, GFDL CM2.0 has a broader peak that encompasses the observed peak, but with the tallest part near 2 yr, indicating a too frequent recurrence of positive and negative phases as also found by Min et al. (2005) and van Oldenborgh et al. (2005). The high and narrow peaks of CCSM3 and FGOALS-g1.0 signify very periodic time series. FGOALS-g1.0 furthermore has relatively tall peaks near 5–6, 9, and 18 months, suggesting some other seasonal mechanisms is driving ENSO variability in this model as compared to the other models and the real world. GISS Atmosphere–Ocean Model (GISS-AOM) also displays peaks near 6 and 12 months, indicating a somewhat annular or semiannular behavior.

Since ENSO has such a strong influence on weather patterns around the world, the fact that the ENSO period for many AOGCMs is too short or too long relative to observations implies that the models' simulation of the timing and frequency of ENSO-related variability in global weather patterns, including the simulated frequency of extreme weather events at the regional scale, could be biased. Likewise, the very periodic component in the CCSM3 and FGOALS-g1.0 models will most likely be reflected in simulated ENSO-related weather patterns,

causing the occurrence of extreme weather to be much less random than in reality in these particular models.

Spectral analysis of ERA-40 and Kaplan-based PDO time series (Fig. 2e) show 3 significant peaks: near 12 months, at 2–4 yr, and a final peak beginning near 7 yr and increasing in power until the end of the analyzed period (480 months). Out of the 19 AOGCMs that provide SST output fields, only GISS-AOM produced spectral peaks similar to those seen in the reanalysis data. The majority of the remaining models display a power spectrum similar in *shape* to reanalysis; however, the peaks are either slightly earlier or slightly later with respect to reanalysis.

In particular, as for ENSO, FGOALS-g1.0 simulations of PDO temporal variability are too periodic and systematic. Also as for ENSO, the fact that some models simulate a too slow or fast oscillation period for PDO will most likely reflect in model-simulated weather patterns affected by the state of the PDO. However, since the PDO oscillates on such a long time scale and is more damped in amplitude than ENSO, this will probably not have such a noticeable effect on model simulations of PDO-related surface weather patterns as might be expected for biased ENSO simulations.

Spectral analysis of the ERA-40 and NCEP reanalysis-based PNA time series (Fig. 2f) show that there are several modes of temporal variability in this pattern. Peaks in reanalysis are found near 4, 6, 12, and 36 months, indicating that the temporal variability of this pattern is dependent on season, but also has a longer (3 yr) component, which is in agreement with PNA oscillation periods documented by the CPC.

Only two out of the 22 AOGCMs [Bjerknes Centre for Climate Research Bergen Climate Model version 2.0 (BCCR-BCM2.0) and UKMO HadCM3] show a periodicity similar to that detected in the reanalysis fields, although neither reproduces the peak at four months. Over half of the AOGCMs reproduce the peak at three years, but there is less agreement among the models about the earlier peaks, which vary from 3 to 18 months. Four models [CGCM3.1 (T63), GFDL CM2.0, GISS-EH, and Parallel Climate Model (PCM)], however, do not reproduce any of the four spectral peaks seen in reanalysis.

The PNA oscillation mainly affects wintertime temperature and precipitation in the United States and Canada, thus the effects of PNA biases would be expected to be observed most during that time. As the PNA is caused by fluctuations in the East Asian jet stream, the implication of biases in PNA simulations suggests a potential lack in the ability of present-day AOGCMs to simulate the dynamics of long-term jet stream fluctuations.

4. Comparison of spatial patterns

We next qualitatively analyze the spatial patterns that result from projecting each time series onto the fields from which they were derived. Seasonal patterns from the historical period 1960–99 for AO and NAO, and the beginning of each model's record to 1999 for AMO, are compared with reanalysis and Kaplan-based patterns to evaluate the models' ability to simulate present-day conditions. Seasonal spatial patterns from the historical period 1960–99 for all patterns are compared with reanalysis-based patterns to evaluate the models' ability to simulate present-day conditions. Only DJF figures are included here (figures for all patterns and seasons as well as tables summarizing the analysis are available at http://temagami.tosm.ttu.edu/~ahertel/teleconnection/), except for the AMO, which are for the entire year. The terminology of the regions analyzed is given in Figs. 1a–f.

a. AOGCM simulation of spatial teleconnection patterns in the Atlantic

The AO teleconnection pattern is located in the mid–high latitudes of the Northern Hemisphere. As illustrated by reanalysis-based patterns (Figs. 3a,b), it consists of a negative anomaly in the 925-hPa geopotential heights near the pole and two positive anomalies generally located in the Atlantic and Pacific regions near 40°N. The region of maximum negative anomaly is slightly stronger in winter with a magnitude between −40 and −50 m.

As shown in Figs. 3c–x, all AOGCMs, with the sole exception of BCC-CM1, clearly simulate a recognizable AO pattern. There is a tendency among the models to underestimate the magnitude of region C1 (regions are shown in Fig. 1), especially in the winter and spring seasons. In winter, several models also simulate a wider C1 area, and the area of the maximum negative values can be shifted to the east. The magnitude of the C2 (North Atlantic) anomaly is underestimated by over half of the models in winter, and nearly half the models in summer. Several models [BCCR-CM2.0, CGCM3.1 (T47), CGCM3.1 (T63), CSIRO Mk3.0, ECHAM5/MPI-OM, GISS-EH, and MIROC3.2 high-resolution version (hires)] display a southward displacement during the winter as well as either a westward or eastward displacement (or both if the region is more spread out, as for CCSM3 and FGOALS-g1.0). Nearly all models produce a C3 region with too large an anomaly for the winter, summer, and fall seasons, whereas almost all models simulate a weaker anomaly for the spring. During the spring, most models displace the C3 region southward, while many displace it northward and westward or eastward in the summer simulations.

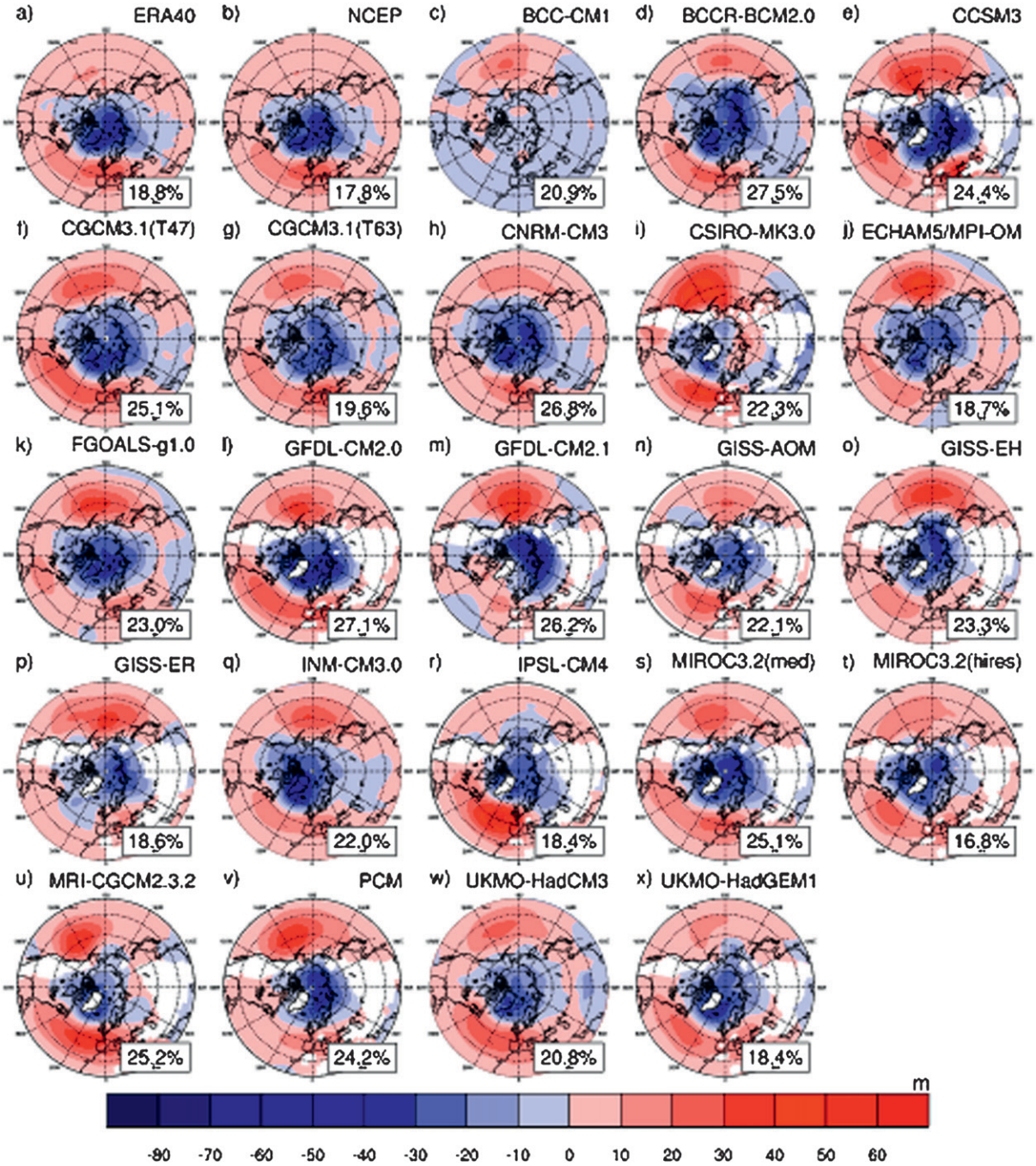

FIG. 3. Reanalysis and AOGCM-based spatial patterns for the AO index for winter (DJF). The percentage of the variance explained by the pattern is given in the lower right-hand corner of each pattern.

None of the AOGCMs is in perfect agreement with observations; however, they all produce a very similar pattern to observed, with BCC-CM1 the only exception. As found by Miller et al. (2006) for the AR4 model simulations as well as by Stephenson et al. (2006) for the CMIP2 simulations, we similarly conclude that the majority of the AR4 models overestimate the percentage of variability explained by the AO pattern (Figs. 3a–x; percentage values in lower right-hand corner). Only ECHAM5/MPI-OM, GISS Model E-R (GISS-ER), IPSL CM4, and UKMO HadGEM1 produce a percentage of explained variance similar to observations, while MIROC3.2(hires) produces a slightly lower percentage of explained variance than observed.

The ability of AOGCMs to simulate weather and climate in the Northern Hemisphere depends on the abilities of the models to reproduce naturally occurring oscillations like the AO. Model biases in simulating the AO, such as too weak or strong centers of the anomalies, or a displacement of the strongest part of the anomaly region, will have an effect on the models' abilities to realistically simulate weather and both current and future climate. Storm tracks and cyclone development may be affected, creating biases in the amount of rainfall received downstream as well as other weather parameters.

The NAO teleconnection pattern is located over the northern part of the Atlantic Ocean. It consists of a region with negative geopotential height anomalies over Greenland and Iceland, with a magnitude of about −80 m and a region of positive geopotential height anomalies near 40°N over the Atlantic Ocean and western Europe with a magnitude near 45 m during the positive phase (Figs. 4a,b).

Most models are able to reproduce a NAO-like pattern during all four seasons. The models that best reproduce the strength and location of both the C1 and C2 regions of the NAO teleconnection pattern are CGCM3.1 (T63), INM-CM3.0, and MIROC3.2, medium-resolution version (medres). The BCC-CM1 and MIROC3.2(hires) models have some difficulty producing a recognizable NAO pattern for spring and summer, while the winter and fall patterns for BCC-CM1 are also questionable.

For DJF and MAM, about half of the models underestimate the magnitude of the C1 region; however, the models that underestimate the magnitude of the C1 region for one season are not necessarily the same for each season. For the C1 region, almost all models are capable of simulating the correct location over southern Greenland, as well as the area of the anomaly, for all four seasons. For the C2 region, approximately half the AOGCMs (although not always the same models) simulate an overly strong and westwardly displaced C2 region in most seasons.

The percentage of variance explained by the NAO is less consistent than for the AO. About half of the models overestimate the percentage of explained variance, whereas nearly half reproduce a reasonable percentage of variability. In particular, CSIRO Mk3.0, GFDL CM2.1, GISS-EH, INM-CM3.0, MIROC3.2(medres), MIROC3.2(hires), and UKMO HadGEM1 produce a percentage of variability similar to observed.

As for the AO, biases in the simulation of the NAO teleconnection pattern likely propagate into AOGCM biases in prediction of climate and weather, particularly over Scandinavia, Europe, eastern North America, and North Africa. Most AOGCMs were able to simulate the location of the two areas of anomalies, except for a general westward displacement of the C2 region. Hence, storm tracks will most likely not be greatly affected by AOGCM biases; however, prediction of the magnitudes of certain weather events, such as rainfall anomalies and the strength of winds, will most likely have biases associated with them for many of the models.

The AMO teleconnection pattern is somewhat different from the AO and NAO patterns not only because it stems from oscillations in ocean temperatures rather than in the atmosphere, but also because the oscillation is more subtle; that is, it has a relatively weak signal compared to the interannual variability or noise and has a much lower frequency, requiring 65–70 yr to complete a cycle. Although the AMO occurs mainly in the North Atlantic, we have included the North Pacific Ocean in figures here because it affects this area as well likely through connection to the thermohaline circulation (Andronova and Schlesinger 2000; Delworth and Mann 2000).

AMO patterns from reanalysis as well as those simulated by the 19 AOGCMs that provided SSTs are shown in Figs. 5a–u, revealing that, even over 120-yr simulations, most models do not reproduce an AMO-like pattern. In the North Atlantic region, only four models [CCSM3, CSIRO Mk3.0, GFDL CM2.1, and MIROC3.2(medres)] produce patterns that resemble observations; GFDL CM2.0, PCM, and UKMO HadCM3 produce patterns that somewhat resemble observations, while the rest do not produce anything similar to observed (see Fig. 9). CCSM3 was the only of these models that also simulated a representative temporal variability.

In all, it appears that the abilities of the AOGCMs to reproduce this pattern are not very good; however, this could be due to the shortness of the period used in the analysis as well as the subtlety of the oscillation, since the amplitude only differs by a few tenths of a degree over 70 yr. Also important are the models' representations of ocean circulation. Many models have a poor simulation of the path of the North Atlantic Current and meridional overturning circulation, which are responsible for a large fraction of the northward oceanic heat transport (Randall et al. 2007).

b. AOGCM simulation of teleconnection spatial patterns in the Pacific

The ENSO pattern is centered in the tropical Pacific Ocean, beginning just off the west coast of South America, and consists of a tongue of warm sea surface water in the tropical Pacific that extends west along the equator to about 160°E originating from the coast of

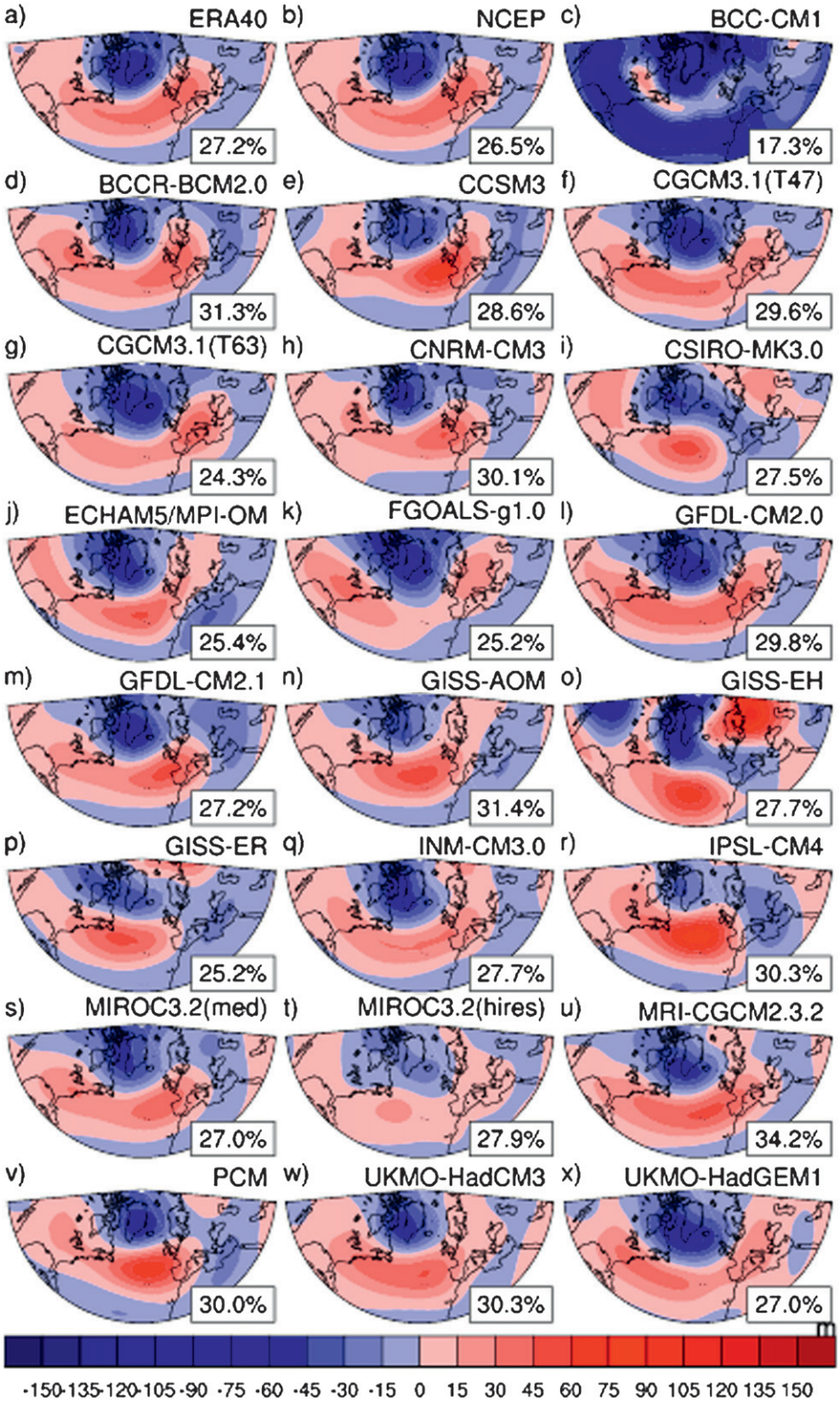

FIG. 4. Reanalysis and AOGCM-based spatial patterns for the NAO index for winter (DJF). The percentage of the variance explained by the pattern is given in the lower right-hand corner of each pattern.

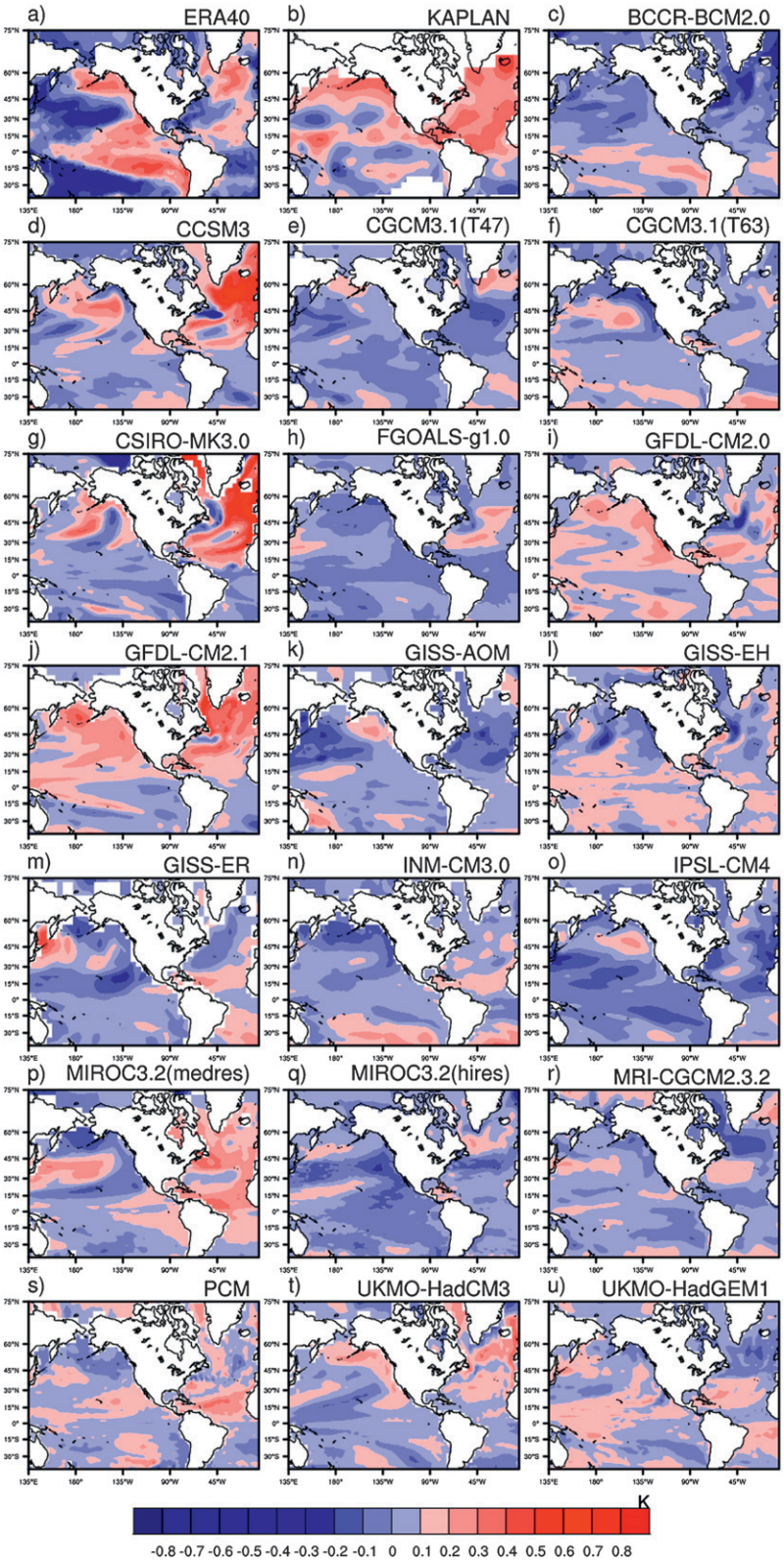

FIG. 5. Reanalysis and AOGCM-based spatial patterns for the annual AMO index based on the full record for each model, all months.

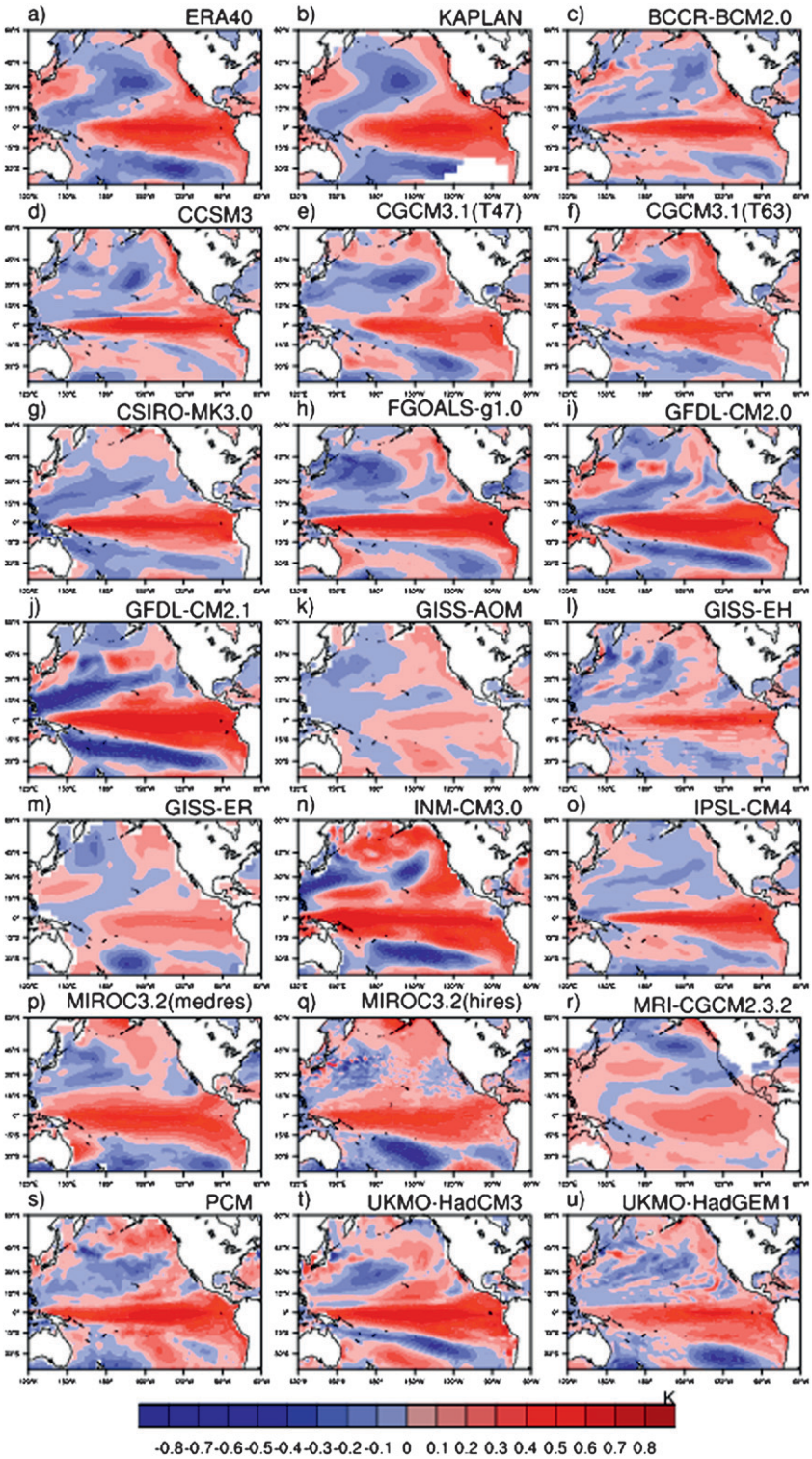

FIG. 6. Reanalysis and AOGCM-based spatial patterns for the ENSO index for winter (DJF).

Peru as well as two cold anomalies north and south of the warm area (Figs. 6a,b). The magnitude of the warm temperature anomaly varies between 1.1 and 1.4 K, with the boreal summer season having the largest anomaly and boreal winter and fall the smallest. Anomalously cold water can be found north and south of the warm tongue. The magnitude of this anomaly is generally around −0.4 K; however, during the boreal spring it increases to about −0.9 K. The location of the southern cold pool varies more with season. It also migrates west from the boreal winter to summer (austral summer to winter) and the magnitude of the anomaly is generally around −0.5 K, except during the austral spring, when it decreases slightly to −0.4 K.

Figs. 6c–u clearly illustrates how all AOGCMs for which SST was available are able to successfully simulate a recognizable ENSO pattern. However, there are some significant differences both among the models and between models and reanalysis. Many models simulate the ENSO SST anomaly centers to be either weaker or stronger in magnitude relative to reanalysis, and many models also show displaced anomaly centers. In particular, there is a general tendency for the models to displace the C1 region farther westward, a result also found in other studies (Cai et al. 2003; Min et al. 2005; van Oldenborgh et al. 2005; Randall et al. 2007).

Out of the 19 AOGCMs for which SST fields were available, only CGCM3.1 (T47), CGCM3.1 (T63), and GISS-ER do not show any westward displacement of the C1 region in any of the seasons. Interestingly, these three are also among the models that consistently underestimate the magnitude of the temperature anomaly in the C1 region. Four models are consistent in underestimating the magnitude of the C1 region (i.e., during three or more seasons), while four others consistently overestimate it. Only 5 out of the 19 models [BCCR-BCM2.0, CSIRO Mk3.0, GISS-EH, MIROC3.2(medres), and PCM] correctly simulate the magnitude of the C1 region in a consistent manner. There is also a tendency among models to underestimate the magnitude of the C2 anomaly during the boreal winter and spring seasons, with 11 and 9 models underestimating the region, respectively, for each of the two seasons. During all four seasons many models also displace the C2 region westward. Finally, the strength of the C3 region, which is located in the southern Pacific, is underestimated by the majority of the models during all four seasons (9, 13, 13, and 15 of the 19 models in DJF, MAM, JJA, and SON, respectively). Throughout the winter, spring, and summer there is a slight tendency for models to displace the C3 region southward and/or eastward. The only models that fail to simulate the C3 region entirely are Meteorological Research Institute Coupled General Circulation Model, version 2.3.2 (MRI CGCM2.3.2) during DJF and GISS-AOM during MAM.

The ability of AOGCMs to simulate weather and climate in both the Northern and Southern Hemispheres depends on the abilities of the models to reproduce naturally occurring oscillations such as ENSO. Model biases in simulating ENSO, such as too weak or strong centers of action, or a displacement of the strongest part of the anomaly region, will affect models' abilities to simulate ENSO-related weather and potential future changes, including tropical precipitation patterns.

The PDO teleconnection pattern is located in the North Pacific and consists of a tongue-shaped region around 35°N, extending from Japan eastward to about 140°W, where SSTs are either anomalously warm or cold, depending on the phase of the pattern; and a region along the west coast of North America, where SST anomalies have the opposite sign of the first region (Figs. 7a,b). The PDO spatial pattern exhibits little seasonal dependence, with the minimum and maximum anomalies of approximately −0.6 and 0.6 K, respectively, regardless of season.

Several of the AOGCMs appear to experience difficulties in simulating a recognizable PDO pattern (Figs. 7c–u). Both the shape and strength of the pattern significantly differ from reanalysis, while for a few models (GISS-EH and GISS-ER) one can even question whether a PDO pattern is simulated at all. Only five models [CGCM3.1 (T47), CGCM3.1 (T63), CSIRO Mk3.0, MIROC3.2(medres), and MIROC3.2(hires)] reproduce a PDO-like pattern similar to reanalysis for all four seasons, with similar shape and strength of the pattern.

There is also a tendency among the AOGCMs to overestimate the strength of the anomaly regions during all four seasons. Out of the 19 models that provided SST, 7 models consistently (i.e., during three or more seasons) overestimate the magnitude of the C1 anomaly; four of these are also consistent in overestimating the magnitude of the C2 region. The three GISS models tend to underestimate the magnitude of the C2 region during three of the four seasons; two might not even be reproducing the correct pattern (as mentioned above), since they also consistently displace the C1 anomaly center a considerable distance to the northwest. BCCR-BCM2.0, INM-CM3.0, and UKMO HadCM3 tend to displace the strongest part of the C1 anomaly westward; however, the remaining models appear relatively successful in locating the anomalies.

The two sets of reanalysis do not quite agree on the value, with ERA-40 attributing only 18.2% of the total variability in SSTs in this region to the PDO, whereas Kaplan attributes 23.2% of the total variability

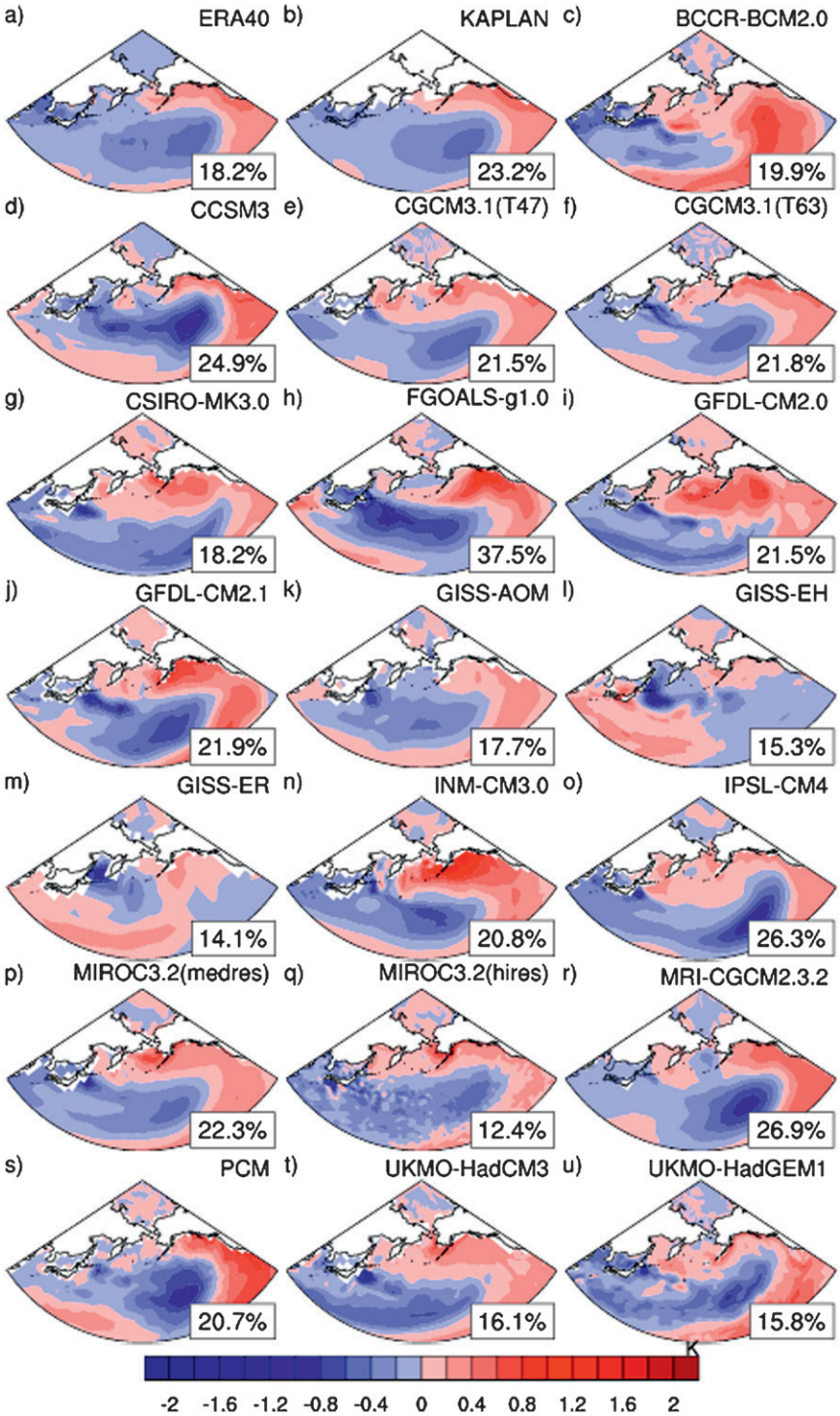

FIG. 7. Reanalysis and AOGCM-based spatial patterns for the PDO index for winter (DJF). The percentage of the variance explained by the pattern is given in the lower right-hand corner of each pattern.

to the PDO (lower right-hand corner of each plot in Fig. 7). The majority of the AOGCMs simulate the amount of percentage variability close to this range, with only a few exceptions. Specifically, FGOALS-g1.0 attributes 37.5% of the variability to PDO, whereas MIROC3.2(hires) is in the other end of the spectrum with only 12.4%. The remaining models are within about four percentage points of reanalysis.

AOGCM difficulties in simulating PDO patterns could be related to the subtlety, that is, low signal-to-noise ratio of the pattern amplitude, and a long period of the oscillation, similar to the AMO. An inability to correctly reproduce the PDO pattern will most likely affect an AOGCM's ability to simulate the relatively slow variations in climate associated with this pattern. However, the PDO pattern mainly affects only long-term variability in SST and climate in the northwestern parts of North America and is not strongly correlated to weather in other parts of the world; hence it is most likely only simulation of longer-term climate variability in these areas that would primarily be impacted.

The PNA pattern consists of a region of positive geopotential height anomaly just southeast of the Aleutian Islands in the North Pacific with a magnitude of about 80 m throughout all seasons (DJF shown in Figs. 8a,b). Another positive anomaly region is located over the eastern United States; however, this region is weaker in magnitude, with an anomaly of 40 m throughout the year. A third region of opposite sign is located in northwestern Canada, with a magnitude of −40 m throughout most of the year. During summer this anomaly migrates into the Arctic Ocean just north of Canada and strengthens in magnitude to −60 m.

With the exception of BCC-CM1 and GISS-EH, all AOGCMs are able to simulate a recognizable DJF PNA spatial pattern (Figs. 8c–x). The BCC-CM1 model appears to simulate the C1 region, but the C2 region is shifted north and C3 region is shifted southwest, whereas GISS-EH has a different shape of the C1 and C3 regions altogether. Model performance is similar during the remaining three seasons.

With the exception of the summer season, there is a tendency for most models to underestimate the strength of the C1 region and overestimate the strength of the C3 region. Specifically, 9 models consistently (i.e., during three or more seasons) simulate a weaker-than-observed C1 region, while 7 correctly simulate the strength of the C1 region. The C2 region is generally simulated correctly during the winter, summer, and fall by the majority of the AOGCMs, both with respect to strength and position. There is a tendency for the models to simulate that the C2 region is located farther east than observed during the spring, with 9 out of the 22 models showing this spring bias. There is also a tendency for the strength of the C3 region to be overestimated by many AOGCMs, with 8 consistently producing a stronger-than-observed C3 anomaly.

ERA-40 and NCEP reanalysis attribute 22.4% and 21.5%, respectively, of the total variability in geopotential heights in this region to the PNA teleconnection pattern (lower right-hand corner of each plot in Fig. 8). Fifteen of the models simulate the percentage of total variability to be 23% or greater, with CCSM3 and FGOALS-g1.0 simulating 30.1% and 32.6% total variability, respectively, to be due to PNA variability.

Biases in the simulation of the PNA teleconnection pattern will likely result in biases in prediction of climate and weather in the regions bordering the North Pacific Ocean, which are affected by the PNA pattern. Most AOGCMs were able to simulate the location of the anomalies, but there was a tendency of models to either under- or overestimate certain anomaly regions, suggesting potential biases in model-simulated storm tracks and prediction of the magnitudes of certain weather events, such as rainfall anomalies and the strength of winds.

5. Conclusions and discussion

From our analysis of the temporal and spatial characteristics of these six teleconnection patterns simulated by the 22 IPCC AR4 AOGCMs for which the required output fields are available, we draw several general conclusions.

First, with only a few exceptions, all of the AOGCMs are able to produce recognizable seasonal spatial patterns for both the AO and the NAO in the North Atlantic region as well as all three patterns in the Pacific region.

For the North Atlantic region, in particular CCSM3, CGCM3.1 (T63), GFDL CM2.0, INM-CM3.0, UKMO HadCM3, and UKMO HadGEM1 produced spatial patterns closely resembling observed patterns, suggesting these are most able to adequately represent the dynamical atmospheric features associated with these patterns, mainly the Northern Hemisphere polar vortex.

For the Pacific region teleconnection patterns, CGCM3.1 (T63) and CSIRO Mk3.0, followed by CGCM3.1 (T47), GFDL CM2.0, MIROC3.2(medres), and MIROC3.2(hires), were most consistent in producing spatial patterns closely resembling the observed patterns, suggesting that these models may represent the dynamical oceanic and atmospheric features associated with these patterns, such as the tropical and North Pacific oceanic dynamics and Northern Hemisphere polar vortex, more successfully than others.

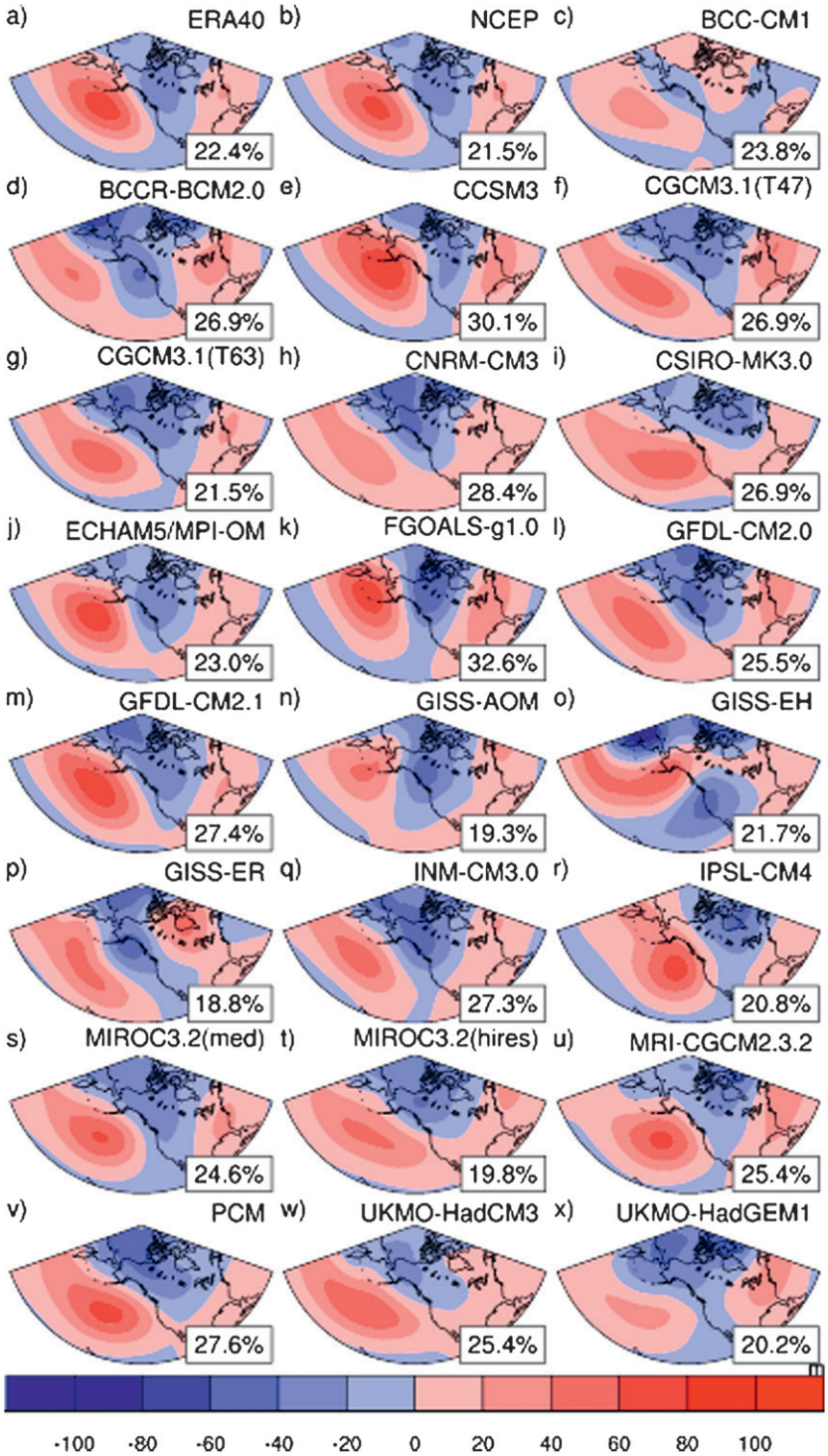

FIG. 8. Reanalysis and AOGCM-based spatial patterns for the annual PNA index for winter (DJF). The percentage of the variance explained by the pattern is given in the lower right-hand corner of each pattern.

There were no consistent biases in the strength of the spatial patterns, with some AOGCMs producing patterns that were too strong in magnitude, while others produced patterns that were too weak. Some models also simulate a displacement in the location of the pattern, which would be expected to affect their ability to simulate the connections between upper-air dynamical patterns and surface climate. These faults may lead to systematic biases in simulation of surface climate patterns known to be associated with upper-air forcing, an issue which remains to be examined in our work to follow.

In contrast, the AOGCMs were not as successful at simulating the longer-period AMO. Only CCSM3, CSIRO Mk3.0, GFDL CM2.1, and MIROC3.2(medres) produced patterns somewhat similar to those seen in the Kaplan dataset. The fact that so few AOGCMs succeeded in reproducing an AMO-like pattern might be associated with the subtleness of the variability, which is only a few fractions of a degree's variation in the ocean surface temperature. It could also be because our analysis only includes a maximum of 150 yr of data, which would only cover two full oscillations. Furthermore, the AMO is a fluctuation in sea surface temperatures; hence ocean circulation plays a vital role in this pattern. However, many models poorly simulate the path of the North Atlantic Current as well as the meridional overturning circulation, which are responsible for a large fraction of the northward oceanic heat transport in the Atlantic Ocean (Randall et al. 2007).

In terms of temporal variability, again most AOGCMs do produce a periodic response of approximately the same order of magnitude as observed—that is, with periods of 6–12 months for the AO and NAO, a few years for ENSO and PNA, and decades for the PDO and AMO. However, most models have difficulties in reproducing the exact temporal characteristics of all teleconnection pattern time series, producing time series that vary either too slowly or too rapidly compared with reanalysis-based time series. A common error is for models to produce time series whose variability is too systematic and periodic, indicating a smaller degree of internal variability in the model as compared to the real world. This was especially true for FGOALS-g1.0.

As found in earlier studies (Miller et al. 2006; Stephenson et al. 2006), the percentage of variability explained by the AO was greater in most cases than that found in reanalysis-based time series. The same is true for the percentage of variability explained by the PNA pattern. More disagreement between the models was found for the NAO than the AO, where about half the AOGCMs overestimated the percentage of variability explained by the pattern, and a little less than half accurately reproduced the percentage of explained variability. For the PDO, the percentage of variability explained was much larger in some models and much smaller in others, compared with reanalysis.

Figure 9 provides a brief summary of model ability to reproduce observed teleconnection patterns and their time series. From this summary we see that the models that produce the best temporal indices are not necessarily the models that produce the best spatial patterns, relative to reanalysis. For example, GISS-EH produces a poor NAO time series but a good NAO spatial pattern. The same is true for INM-CM3.0, which poorly reproduces the AO temporal variability but simulates a good AO spatial pattern. ENSO, BCCR-CM2.0, CGCM3.1 (T63), and CSIRO Mk3.0 produce a poor time series but a good ENSO spatial pattern. Similarly, CGCM3.1 (T63) and PCM, which poorly reproduce the PNA temporal variability, simulate a good PNA spatial pattern.

In general, considering the overall ability of the models to simulate both the temporal and spatial variability of the six patterns, the most capable models appear to be the CCSM3, CSIRO Mk3.0, CGCM3.1 (T63), GFDL CM2.0 and 2.1, HadCM3, HadGEM1, MIROC3.2(medres), and PCM models, while BCC-CM1, FGOALS-g1.0, GISS-EH, and GISS-ER tend to be some of the least successful models.

One might be able to hold spatial resolution responsible for some model deficiencies. For example, FGOALS-g1.0, GISS-AOM, GISS-EH, GISS-ER, INM-CM3.0, and IPSL CM4 time and again produced poor results, specifically in the Pacific region and for the AMO. These six models vary in resolution of the atmospheric component between $2.8° \times 2.8°$ for FGOALS-g1.0 to $4° \times 5°$ for the GISS family of models. The models also have poor resolution for the ocean component (Table 1). However, not all the fault can be placed on resolution alone, since the BCC-CM1 model, which has excellent resolution ($1.9° \times 1.9°$, for both atmospheric and oceanic components) consistently failed in the analysis, whereas MIROC3.2(medres) and UKMO HadCM3, which have relatively coarse resolution ($2.8° \times 2.8°$ and $2.5° \times 3.75°$ for the atmospheric component, respectively) produced results comparable with the better range of models. Hence part of the deficiencies of some of the models must lie in the parameterization of atmospheric physics within the models. This could be coupling between the atmosphere and ocean or the atmosphere and land, or how schemes such as clouds, convection, radiative transfer, and boundary layer regimes are incorporated in each model. With so many models we were obviously not able to get into the depth that single-index studies such as, for example, AchutaRao and Sperber (2006) did for ENSO, but exactly how the atmospheric physics of the models is lacking clearly remains a subject to

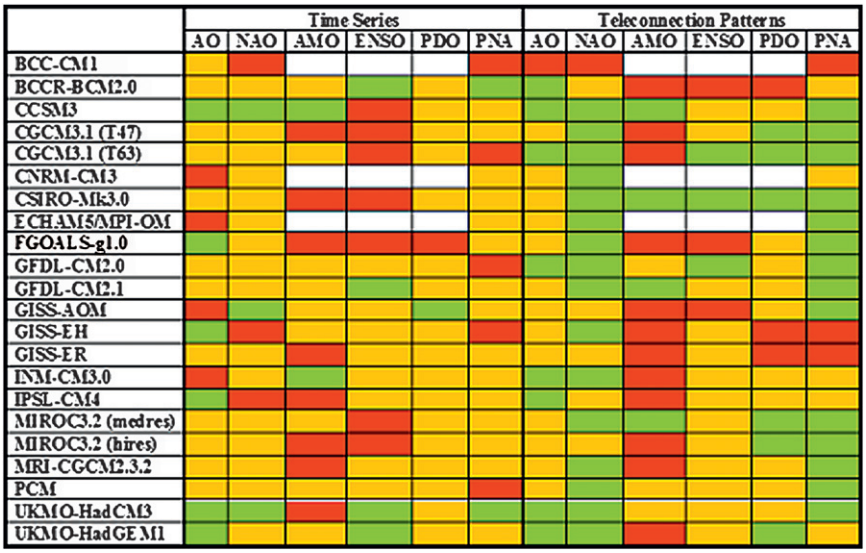

FIG. 9. Summary of model performance in simulating historical observed teleconnection patterns and their time series indices. Green indicates the model is capable of reproducing a spatial or temporal pattern that closely resembles the observations. Orange indicates the model is able to produce a recognizable temporal or spatial pattern, albeit one with significant differences relative to the observations. Red indicates the model is not able to produce a recognizable temporal or spatial pattern. White indicates insufficient model data were available to make the comparison.

be examined to be able to use these results to guide model improvements.

Atmospheric chemistry and aerosols can also affect model performance. It is interesting to note that most of the models that perform well in this analysis include atmospheric chemistry: CCSM3, ECHAM5/MPI-OM, UKMO HadCM3, and UKMO HadGEM1. In contrast, poorer-performing models such as BCC-CM1, FGOALS-g1.0, GISS-AOM, GISS-EH, and GISS-ER do not. We have no evident answers as to why this is the case; it could be that the chemistry component in the models has feedbacks to radiative heating and/or dynamics, or that models that include chemistry and aerosols also have better physical parameterizations of heat exchange. This remains to be examined in detail.

Furthermore, many of the low-resolution models only include sulfate aerosols, whereas more sophisticated and successful models (CCSM3, GFDL CM2.0, GFDL CM2.1, and HadGEM1) include more aerosol particles such as dust, sea salt, and black and organic carbon as well as stratospheric volcanic aerosols.

This analysis provides a systematic assessment of the ability of current AOGCMs to simulate natural variability of the recent historical period and identifies some common biases in simulation of both the spatial and temporal characteristics of these natural cycles. We cannot say that one model is necessarily better than the others, since all differ in their ability to reproduce the teleconnection patterns and associated time series, and successful simulation of one teleconnection pattern does not necessarily mean that another will be reproduced as well. However, we hope this analysis will provide guidance regarding selection of appropriate models to study climate over a specific region, depending on which teleconnection pattern is most closely linked to climate over that region and the ability of the model to simulate that specific pattern. Further research focusing on individual models is needed to identify specific aspects of their dynamics and physics that may be responsible for causing the biases identified here as well as to assess the ability of AOGCMs to simulate the correlation of these teleconnection patterns with surface climate anomalies around the globe.

Acknowledgments. We thank Jeff van Dorn for data assistance and Claudia Tebaldi for insight into statistical analysis techniques. We acknowledge the international modeling groups for providing data for analysis, the Program for Climate Model Diagnosis and Intercomparison (PCMDI) for collecting and archiving the model data, the WCRP and JSC/CLIVAR Working Group on Coupled Modelling (WGCM) and their Coupled Model Intercomparison Project (CMIP) and Climate Simulation Panel for organizing model data analysis activity, and the IPCC WG1 TSU for technical support. Although this research has been funded wholly or in part by the United

States National Science Foundation DMS Cooperative Agreement #07-24752 to the University of Illinois as well as the United States Environmental Protection Agency through STAR Cooperative Agreement #R-82940201 to the University of Chicago, it has not been subjected to USNSF or USEPA peer and policy review; it therefore does not necessarily reflect the views of USNSF or USEPA, and no official endorsement should be inferred.

REFERENCES

AchutaRao, K., and K. R. Sperber, 2002: Simulation of the El Niño southern oscillation: Results from the Coupled Model Intercomparison Project. *Climate Dyn.,* **19,** 191–209.

——, and ——, 2006: ENSO simulation in coupled ocean-atmosphere models: Are the current models better? *Climate Dyn.,* **27,** 1–15, doi:10.1007/s00382-006-0119-7.

Ambaum, M. H. P., B. J. Hoskins, and D. B. Stephenson, 2001: Arctic Oscillation or North Atlantic Oscillation? *J. Climate,* **14,** 3495–3507.

Andronova, N. G., and M. E. Schlesinger, 2000: Causes of global temperature changes during the 19th and 20th centuries. *Geophys. Res. Lett.,* **27,** 2137–2140.

Barnston, A. G., and R. E. Livezey, 1987: Classification, seasonality and persistence of low-frequency atmospheric circulation patterns. *Mon. Wea. Rev.,* **115,** 1083–1126.

Bjerknes, J., 1964: Atlantic air-sea interaction. *Adv. Geophys.,* **10,** 1–82.

Bojariu, R., and L. Gimeno, 2003: Predictability and numerical modelling of the North Atlantic Oscillation. *Earth Sci. Rev.,* **63,** 145–168.

Cai, W., M. A. Collier, H. B. Gordon, and L. J. Waterman, 2003: Strong ENSO variability and a super-ENSO pair in the CSIRO Mark 3 coupled climate model. *Mon. Wea. Rev.,* **131,** 1189–1210.

Cohen, J., A. Frei, and R. D. Rosen, 2005: The role of boundary conditions in AMIP-2 simulations of the NAO. *J. Climate,* **18,** 973–981.

Collins, W. D., and Coauthors, 2006: The Community Climate System Model Version 3 (CCSM3). *J. Climate,* **19,** 2122–2143.

Corti, S., A. Giannini, S. Tibaldi, and F. Molteni, 1997: Patterns of low-frequency variability in a three-level quasigeostrophic model. *Climate Dyn.,* **13,** 883–904.

Covey, C., K. M. AchutaRao, U. Cubasch, P. Jones, S. J. Lambert, M. E. Mann, T. J. Phillips, and K. E. Taylor, 2003: An overview of results from the Coupled Model Intercomparison Project. *Global Planet. Change,* **37,** 103–133.

CSMD, 2005: An introduction to the first-generation operational climate model at National Climate Center. Advances in Climate System Modeling, Vol. 1, 14 pp.

Davey, M., and Coauthors, 2002: STOIC: A study of coupled model climatology and variability in tropical ocean regions. *Climate Dyn.,* **18,** 403–420.

Delworth, T. L., and M. E. Mann, 2000: Observed and simulated multidecadal variability in the Northern Hemisphere. *Climate Dyn.,* **16,** 661–676.

——, and Coauthors, 2006: GFDL's CM2 global coupled climate models. Part I: Formulation and simulation characteristics. *J. Climate,* **19,** 643–674.

Derome, J., H. Lin, and G. Brunet, 2005: Seasonal forecasting with a simple general circulation model: Predictive skill in the AO and PNA. *J. Climate,* **18,** 597–609.

Diansky, N. A., and E. M. Volodin, 2002: Simulation of the present-day climate with a coupled atmosphere-ocean general circulation model. *Izv. Atmos. Ocean. Phys.,* **38,** 732–747.

——, A. V. Bagno, and V. B. Zalesny, 2002: Sigma model of global ocean circulation and its sensitivity to variations in wind stress. *Izv. Atmos. Ocean. Phys.,* **38,** 477–494.

Enfield, D. B., A. M. Mestas-Nuñez, and P. J. Trimble, 2001: The Atlantic multidecadal oscillation and its relation to rainfall and river flows in the continental U.S. *Geophys. Res. Lett.,* **28,** 2077–2080.

Flato, G. M., cited 2005: The Third Generation Coupled Global Climate Model (CGCM3). [Available online at http://www.cccma.bc.ec.gc.ca/models/cgcm3.shtml.]

Furevik, T., M. Bentsen, H. Drange, I. K. T. Kindem, N. G. Kvamstø, and A. Sorteberg, 2003: Description and evaluation of the Bergen climate model: ARPEGE coupled with MICOM. *Climate Dyn.,* **21,** 27–51.

Gordon, C., C. Cooper, C. A. Senior, H. T. Banks, J. M. Gregory, T. C. Johns, J. F. B. Mitchell, and R. A. Wood, 2000: The simulation of SST, sea ice extents and ocean heat transports in a version of the Hadley Centre coupled model without flux adjustments. *Climate Dyn.,* **16,** 147–168.

Gordon, H. B., and Coauthors, 2002: The CSIRO Mk3 Climate System Model. CSIRO Atmospheric Research Tech. Paper 60, 134 pp. [Available online at http://www.cmar.csiro.au/e-print/open/gordon_2002a.pdf.]

Graham, R. J., M. Gordon, P. J. McLean, S. Ineson, M. R. Huddleston, M. K. Davey, A. Brookshaw, and R. T. Barnes, 2005: A performance comparison of coupled and uncoupled versions of the Met Office seasonal prediction general circulation model. *Tellus,* **57A,** 320–339.

Guilderson, T. P., and D. P. Schrag, 1998: Abrupt shift in subsurface temperatures in the tropical Pacific associated with changes in El Niño. *Science,* **281,** 240–243.

Hasumi, H., and S. Emori, 2004: K-1 coupled GCM (MIROC) description. K-1 Tech. Rep. 1, Center for Climate System Research, University of Tokyo, 39 pp. [Available online at http://www.ccsr.u-tokyo.ac.jp/kyosei/hasumi/MIROC/tech-repo.pdf.]

Hourdin, F., and Coauthors, 2006: The LMDZ4 general circulation model: Climate performance and sensitivity to parameterized physics with emphasis on tropical convection. *Climate Dyn.,* **27,** 787–813.

Hurrell, J. W., 1995: Decadal trends in the North Atlantic Oscillation: Regional temperature and precipitation. *Science,* **269,** 676–679.

——, 1996: Influence of variations in extratropical wintertime teleconnections on Northern Hemisphere temperature. *Geophys. Res. Lett.,* **23,** 665–668.

——, J. J. Hack, A. S. Phillips, J. Caron, and J. Yin, 2006: The dynamical simulation of the Community Atmosphere Model Version 3 (CAM3). *J. Climate,* **19,** 2162–2183.

Huth, R., 1997: Continental-scale circulation in the UKHI GCM. *J. Climate,* **10,** 1545–1561.

Johns, T. C., and Coauthors, 2006: The new Hadley Centre climate model HadGEM1: Evaluation of coupled simulations. *J. Climate,* **19,** 1327–1353.

Kållberg, P., A. Simmons, S. Uppala, and M. Fuentes, 2004: The ERA-40 archive. ERA-40 Project Rep. Ser 7, ECMWF, 31 pp. [Available online at http://www.ecmwf.int/publications/library/ecpublications/_pdf/era40/ERA40_PRS17_rev1.pdf.]

Kaplan, A., M. Cane, Y. Kushnir, A. Clement, M. Blumenthal, and B. Rajagopalan, 1998: Analyses of global sea surface temperature 1856-1991. *J. Geophys. Res.,* **103,** 18 567–18 589.

Karspeck, A. R., and M. A. Cane, 2002: Tropical Pacific 1976–77 climate shift in a linear, wind-driven model. *J. Phys. Oceanogr.,* **32,** 2350–2360.

Kerr, R. A., 2000: A North Atlantic climate pacemaker for the centuries. *Science,* **288,** 1984–1985.

Kestin, T. S., D. J. Karoly, J.-I. Yano, and N. A. Rayner, 1998: Time-frequency variability of ENSO and stochastic simulations. *J. Climate,* **11,** 2258–2272.

Knight, J. R., C. K. Folland, and A. A. Scaife, 2006: Climate impacts of the Atlantic Multidecadal Oscillation. *Geophys. Res. Lett.,* **33,** L17706, doi:10.1029/2006GL026242.

Kodera, K., and Y. Kuroda, 2004: Two teleconnection patterns involved in the North Atlantic/Arctic Oscillation. *Geophys. Res. Lett.,* **31,** L20201, doi:10.1029/2004GL020933.

Kutzbach, J. E., 1970: Large-scale features of monthly mean Northern Hemisphere anomaly maps of sea-level pressure. *Mon. Wea. Rev.,* **98,** 708–716.

Latif, M., and Coauthors, 2001: ENSIP: The El Niño simulation intercomparison project. *Climate Dyn.,* **18,** 255–276.

Li, Z.-X., 1999: Ensemble atmospheric GCM simulation of climate interannual variability from 1979 to 1994. *J. Climate,* **12,** 986–1001.

Lorenz, E. N., 1950: Seasonal and irregular variations of the Northern Hemisphere sea-level pressure profile. *J. Meteor.,* **8,** 52–59.

Mantua, N. J., S. R. Hare, Y. Zhang, J. M. Wallace, and R. C. Francis, 1997: A Pacific interdecadal climate oscillation with impacts on salmon production. *Bull. Amer. Meteor. Soc.,* **78,** 1069–1079.

Martin, G. M., M. A. Ringer, V. D. Pope, A. Jones, C. Dearden, and T. J. Hinton, 2006: The physical properties of the atmosphere in the new Hadley Centre Global Environmental Model (HadGEM1). Part I: Model description and global climatology. *J. Climate,* **19,** 1274–1301.

McHugh, M. J., and J. C. Rogers, 2005: Multi-model representation of the North Atlantic Oscillation in the 20th and 21st centuries. *Geophys. Res. Lett.,* **32,** L21713, doi:10.1029/2005GL023679.

Mestas-Nuñez, A. M., and D. B. Enfield, 1999: Rotated global modes of non-ENSO sea surface temperature variability. *J. Climate,* **12,** 2734–2746.

Miller, R. L., G. A. Schmidt, and D. T. Shindell, 2006: Forced annular variations in the 20th century Intergovernmental Panel on Climate Change Assessment Report models. *J. Geophys. Res.,* **111,** D18101, doi:10.1029/2005JD006323.

Min, S.-K., S. Legutke, A. Hense, and W.-T. Kwon, 2005: Internal variability in a 1000-yr control simulation with the coupled climate model ECHO-G—II. El Niño Southern Oscillation and North Atlantic Oscillation. *Tellus,* **57A,** 622–640.

Nigam, S., M. Barlow, and E. H. Berbery, 1999: Analysis links Pacific decadal variability to drought and streamflow in United States. *Eos, Trans. Amer. Geophys. Union,* **80** (51), 621.

Nitta, T., and S. Yamada, 1989: Recent warming of tropical sea surface temperature and its relationship to Northern Hemisphere circulation. *J. Meteor. Soc. Japan,* **67,** 187–193.

Osborn, T. J., K. R. Briffa, S. F. B. Tett, P. D. Jones, and R. M. Trigo, 1999: Evaluation of the North Atlantic Oscillation as simulated by a coupled climate model. *Climate Dyn.,* **15,** 685–702.

Overland, J. E., and M. Wang, 2007: Future climate of the North Pacific Ocean. Eos, *Trans. Amer. Geophys. Union,* **88,** 178–182.

Pope, V. D., M. L. Gallani, P. R. Rowntree, and R. A. Stratton, 2000: The impact of new physical parametrizations in the Hadley Centre climate model: HadAM3. *Climate Dyn.,* **16,** 123–146.

Quinn, W. H., and V. T. Neal, 1984: Recent climate change and the 1982-83 El Niño. *Proc. Eighth Annual Climate Diagnostic Workshop,* Downsville, ON, Canada, NOAA, 148–154.

——, and ——, 1985: Recent long-term climate change over the eastern tropical subtropical Pacific and its ramifications. *Proc. Ninth Annual Climate Diagnostic Workshop,* Corvallis, OR, NOAA, 101–109.

Randall, D. A., and Coauthors, 2007: Climate models and their evaluation. *Climate Change 2007: The Physical Science Basis,* S. Solomon et al., Eds., Cambridge University Press, 589–662.

Roeckner, E., and Coauthors, 2003: The atmospheric general circulation model ECHAM 5. Part I: Model description. Max-Planck-Institute for Meteorology Rep., 127 pp. [Available online at http://edoc.mpg.de/175329.]

Rogers, J. C., and M. J. McHugh, 2002: On the separability of the North Atlantic oscillation and the Arctic oscillation. *Climate Dyn.,* **19,** 599–608.

Russell, G. L., cited 2005: 4x3 atmosphere-ocean model documentation. [Available online at http://aom.giss.nasa.gov/doc4x3.html.]

——, J. R. Miller, and D. Rind, 1995: A coupled atmosphere-ocean model for transient climate change studies. *Atmos.–Ocean,* **33,** 683–730.

Salas-Mélia, and Coauthors, 2005: Description and validation of the CNRM-CM3 global coupled model. CNRM Working Note 103, 36 pp.

Schlesinger, M. E., and N. Ramankutty, 1994: An oscillation in the global climate system of period 65-70 years. *Nature,* **367,** 723–726.

Schmidt, G. A., and Coauthors, 2006: Present-day atmospheric simulations using GISS ModelE: Comparison to in situ, satellite, and reanalysis data. *J. Climate,* **19,** 153–192.

Schoof, J. T., and S. C. Pryor, 2006: An evaluation of two GCMs: Simulation of North American teleconnection indices and synoptic phenomena. *Int. J. Climatol.,* **26,** 267–282.

Smith, C. A., and P. Sardeshmukh, 2000: The effect of ENSO on the intraseasonal variance of surface temperature in winter. *Int. J. Climatol.,* **20,** 1543–1557.

Stephenson, D. B., and V. Pavan, 2003: The North Atlantic Oscillation in coupled climate models: A CMIP1 evaluation. *Climate Dyn.,* **20,** 381–399.

——, ——, M. Collins, M. M. Junge, and R. Quadrelli, 2006: North Atlantic Oscillation response to transient greenhouse gas forcing and the impact on European winter climate: A CMIP2 multi-model assessment. *Climate Dyn.,* **27,** 401–420.

Sterl, A., 2004: On the (in)homogeneities of reanalysis products. *J. Climate,* **17,** 3866–3873.

Straus, E. M., and J. Shukla, 2002: Does ENSO force the PNA? *J. Climate,* **15,** 2340–2358.

Thompson, D. W. J., and J. M. Wallace, 1998: The Arctic Oscillation signature in the wintertime geopotential height and temperature fields. *Geophys. Res. Lett.,* **25** (9), 1297–1300.

Timmermann, A., J. Oberhuber, A. Bacher, M. Esch, M. Latif, and E. Roeckner, 1999: Increased El Niño frequency in a climate model forced by future greenhouse warming. *Nature,* **398,** 694–697.

Trenberth, K. E., 1997: The definition of El Niño. *Bull. Amer. Meteor. Soc.,* **78,** 2771–2777.

——, and D. A. Paolino Jr., 1981: Characteristic patterns of variability of sea level pressure in the Northern Hemisphere. *Mon. Wea. Rev.,* **109,** 1169–1189.

——, and T. J. Hoar, 1996: The 1990–1995 El Niño-Southern Oscillation event: Longest on record. *Geophys. Res. Lett.,* **23,** 57–60.

Trigo, I. F., 2006: Climatology and interannual variability of storm-tracks in the Euro-Atlantic Sector: A comparison between ERA-40 and NCEP/NCAR reanalyses. *Climate Dyn.,* **26,** 127–143.

van Loon, H., and J. C. Rogers, 1978: The seesaw in winter temperatures between Greenland and northern Europe. Part I: General description. *Mon. Wea. Rev.,* **106,** 296–310.

van Oldenborgh, G. J., S. Y. Philip, and M. Collins, 2005: El Niño in a changing climate: A multi-model study. *Ocean Sci.,* **1,** 81–95.

Walker, G. T., 1923: Correlation in seasonal variations of weather. VIII. A preliminary study of world-weather. *Mem. Indian Meteor. Dep.,* **24** (Part 4), 75–131.

——, and E. W. Bliss, 1932: World weather V. *Mem. Roy. Meteor. Soc.,* **4,** 53–84.

Wallace, J. M., and D. S. Gutzler, 1981: Teleconnections in the geopotential height field during the Northern Hemisphere winter. *Mon. Wea. Rev.,* **109,** 784–812.

Wang, B., and Y. Wang, 1996: Temporal structure of the Southern Oscillation as revealed by waveform and wavelet analysis. *J. Climate,* **9,** 1586–1598.

Wang, M., J. E. Overland, and N. A. Bond, 2009: Climate projections for selected large marine ecosystems. *J. Mar. Syst.,* in press.

Washington, W. M., and Coauthors, 2000: Parallel Climate Model (PCM) control and transient simulations. *Climate Dyn.,* **16,** 755–774.

Yu, Y., R. Yu, X. Zhang, and H. Liu, 2002: A flexible global coupled climate model. *Adv. Atmos. Sci.,* **19,** 169–190.

——, X. Zhang, and Y. Guo, 2004: Global coupled ocean–atmosphere general circulation models in LASG/IAP. *Adv. Atmos. Sci.,* **21,** 444–455.

Yukimoto, S., and A. Noda, 2003: Improvements of the Meteorological Research Institute Global Ocean-Atmosphere Coupled GCM (MRI-GCM2) and its climate sensitivity. CGER's Supercomputing Activity Rep., Vol. 10-2001, National Institute for Environmental Studies, Ibaraki, Japan, 37–44.

——, and Coauthors, 2001: The new Meteorological Research Institute global ocean-atmosphere coupled GCM (MRI-CGCM2)–Model climate and variability. *Pap. Meteor. Geophys.,* **51,** 47–88.

Zhang, Y., J. M. Wallace, and D. S. Battisti, 1997: ENSO-like interdecadal variability: 1900–93. *J. Climate,* **10,** 1004–1020.